ACCSCIENCE PUBLISHING

International Journal of Bioprinting

RESEARCH ARTICLE

Development and validation of a low-cost, open-source robotic extrusion printing platform for acellular hydrogel scaffold fabrication: A step toward multi-axis robotic bioprinting

Kenneth Houston, Perrin Woods, and Ahasan Habib*

Department of Mechanical and Mechatronics Engineering Technology, College of Engineering Technology, Rochester Institute of Technology, Rochester, New York, United States of America

Abstract

Commercial multi-axis robotic bioprinting platforms remain prohibitively expensive for many laboratories, limiting access to robot-assisted biofabrication. This study converted a low-cost six-axis industrial robot (ABB IRB 120T with IRC5 Compact controller) into an open-source robotic extrusion printing platform and compared its dimensional performance with a commercial robotic bioprinter (BioAssemblyBot 400). Validation was limited to acellular hydrogel and planar toolpaths; cell-laden and non-planar printing remain necessary for biological validation. The platform integrated a modified printhead, elevated glass print bed, solenoid-based extrusion control, and a software pipeline that translated slicer-generated G-code into ABB RAPID motion and I/O commands. Five scaffolds were printed using the developed platform and three using the commercial system with a 4% alginate–4% carboxymethylcellulose bioink. The retrofitted platform demonstrated higher repeatability, with a mean coefficient of variation of 2.25% and maximum dimensional range of 0.388 mm, compared with 5.07% and 1.130 mm for the commercial system. Scaffold-level analysis ($n = 5$ vs. $n = 3$) showed significantly lower macro-scale dimensional variance for the retrofitted system, while pore-scale variance was lower but not statistically significant. No statistically significant difference between platforms was detected for overall-dimension or Y-direction pore-width accuracy, whereas the retrofitted system showed better X-direction pore-length accuracy in the pooled analysis. The total development cost was $16,617, an 89.6% reduction relative to the commercial system. These findings demonstrate a technically viable, substantially lower-cost pathway to multi-axis robotic biofabrication, with remaining dimensional limitations likely tied to bioink processing and the absence of crosslinking rather than robotic motion control.

Keywords: Extrusion bioprinting; Robotic bioprinting; Six-axis industrial robot; G-code-to-RAPID translation; Open-source bioprinter; Dimensional accuracy validation

***Corresponding author:**
Ahasan Habib
(mahmet@rit.edu)

Citation: Houston K, Woods P, Habib A. Development and validation of a low-cost, open-source robotic extrusion printing platform for acellular hydrogel scaffold fabrication: A step toward multi-axis robotic bioprinting. *Int J Bioprint*.
doi: 10.36922/IJB026330352

Received: August 10, 2026

Revised: October 15, 2026

Accepted: October 15, 2026

Published online: November 18, 2026

Copyright: © 2026 Author(s). This is an Open-Access article distributed under the terms of the Creative Commons Attribution License, permitting distribution, and reproduction in any medium, provided the original work is properly cited.

Publisher's Note: AccScience Publishing remains neutral with regard to jurisdictional claims in published maps and institutional affiliations.

1. Introduction

Three-dimensional (3D) bioprinting is an additive manufacturing process that deposits bioinks—biomaterials combined with living cells—to fabricate scaffolds and

constructs that replicate features of native tissue. As a bottom-up tissue engineering technique, it enables precise, reproducible control of cell distribution at the micrometer scale and is increasingly used in regenerative medicine, drug screening, and disease modeling.[1] Extrusion is the dominant fabrication method in commercial and research bioprinters: it accommodates a wide range of hydrogel viscosities[2-4] and supports continuous strand deposition, at the cost of shear stress on encapsulated cells during flow through the nozzle.[5-7] Despite this maturity, cost remains one of the largest barriers to adoption; commercial bioprinting systems commonly cost tens of thousands of dollars before accounting for the temperature-controlled enclosures, sterility infrastructure, and cell-culture equipment a working lab requires.[8]

Nearly all low-cost bioprinting solutions to date, including hybrid systems built on desktop fused-deposition-modeling (FDM) gantries, remain confined to Cartesian, three-axis motion.[9,10] Cartesian kinematics are well suited to simple planar geometries but are fundamentally limited when a toolpath must follow a curved, non-planar surface or reach into a confined defect geometry—constraints that become central in *in situ* bioprinting, where bioink is deposited directly onto or within a patient-specific tissue defect during a procedure rather than printed *ex vivo* and implanted afterward. Multi-axis serial manipulators—six-axis industrial robotic arms in particular—relax these constraints by allowing tool orientation to track an arbitrary surface normal, and continuum/soft-robotic *in situ* bioprinters have demonstrated this advantage directly, delivering multilayer bioink through flexible, endoscope-compatible arms for internal, non-planar deposition.[11]

Beyond bioprinting, multi-axis robotic arms are already an established platform for the non-planar capability requested above: directed energy deposition and other robot-assisted additive manufacturing processes are frequently performed on six-axis (or higher) industrial arms because conformal, non-planar toolpaths are required on curved or built-up substrates.[12] At the opposite end of the cost spectrum, low-cost parallel-kinematic (Delta) robot architectures have also been proposed as an affordable alternative to serial industrial arms,[13] though Delta kinematics retain only three translational degrees of freedom and cannot reorient the tool relative to the substrate, unlike the six-axis platform used here. Most directly relevant to the present work, Shojaei Barjuei *et al.*[14] recently used a six-axis collaborative arm (UR5e) to print on curved and angled surfaces with dynamic nozzle-orientation tracking, reducing surface roughness by more than half (28.7 μm vs. 63.4 μm) relative to three-axis printing of the same geometry—direct, quantitative evidence of the advantage six-axis kinematics can provide once a platform's translation and process pipeline are validated. The present study targets that same six-axis platform class but, as detailed in Section 4.4, deliberately validates it first in Cartesian-equivalent (planar) mode, isolating the G-code-to-RAPID translation pipeline from confounding kinematic variables before non-planar toolpaths are attempted.

A growing body of work has explored industrial robotic arms specifically for bioprinting. Yang *et al.*[15] mounted a syringe-based extrusion tool with a structured-light scanning system on a seven-degree-of-freedom KUKA LBR iiwa, achieving a global positional error below 120 μm on planar toolpaths generated through the Robot Operating System. Albrecht *et al.*[16] built a custom syringe-extrusion printhead with an integrated ionic/photo dual-crosslinking module for an ABB IRB 120—the same robot family retrofitted in the present study—and validated print accuracy against the source computer-aided design (CAD) model, though the imaging methodology used to obtain those measurements was not reported and testing was limited to planar and angled surfaces. Both platforms, however, were purpose-built for a single robot: neither could also drive a conventional FDM printer, and neither study addressed the cost of the software required to generate robot motion from a standard slicer output. Fortunato *et al.*[17] took a complementary, fully custom-hardware approach with IMAGObot, a five-degree-of-freedom, largely 3D-printed open-source robotic platform controlled through LinuxCNC and MATLAB path planning, and used it to demonstrate *in situ* photo-crosslinking and reconstruction of a patient-specific cranial defect with a mean trajectory error of 1.38 ± 0.37 mm.[18] IMAGObot lowers cost substantially but, like the industrial-arm studies above, is not compatible with the existing FDM/slicer software ecosystem and has one fewer degree of freedom than the IRB 120T used here.[16-18] Vision-based correction of printed toolpaths—most recently demonstrated by Shojaei Barjuei *et al.*,[19] who used computer vision to detect and compensate for filament placement error in real time, reducing layer-width disparity from 0.6 mm to 0.15 mm—represents an orthogonal strategy for improving robotic bioprinting accuracy that is compatible with, rather than a substitute for, the kinematic retrofit approach taken here.

A second, largely separate barrier is software: standard 3D-printer G-code, generated by slicing an STL file, is not natively understood by industrial robot controllers, which are programmed in vendor-specific languages such as ABB's RAPID. Commercial G-code-to-RAPID solutions exist—ABB's 3D Printing PowerPac add-in and the

RoboDK machining/welding project—but both require paid, proprietary software (PowerPac carries a subscription cost of roughly $1,900/year; RoboDK is a one-time purchase near $4,000), which works directly against the goal of lowering the cost of entry to robotic bioprinting.[20,21] Custom, non-commercial translators have also been reported: Nilsson[22] developed a RobotStudio add-in that converts ISO 6983 G-code to RAPID targets for offline programming, and Pan *et al.*[23] developed an analogous offline G-code parser, "Robmach," for the free RoboWork simulation environment. Both are effective, but both are offline programming tools that generate a static robot path before printing or machining begins; neither intercepts and translates G-code in real time during execution, and neither has been validated on a bioprinting task.

To the best of our knowledge, this work addresses a gap at the intersection of three unmet needs. Specifically, no previously reported system has simultaneously combined (i) the positional repeatability of an unmodified, commercially available industrial robot, (ii) a real-time, open-source G-code-to-RAPID translation pipeline that preserves compatibility with the existing FDM slicer/G-code ecosystem rather than requiring a custom robot-specific toolchain, and (iii) a statistically rigorous, head-to-head experimental validation against a commercial robotic bioprinting platform. In this work, we retrofit a low-cost, previously non-bioprinting six-axis industrial manipulator (ABB IRB 120T/IRC5 Compact) with an inhouse extrusion printhead,[24,25] develop a real-time OctoPrint plugin and RAPID program that translate G-code to robot motion over a two-stage transmission control protocol/internet protocol (TCP/IP) handshake, and validate the resulting platform's dimensional accuracy and repeatability against a commercial robotic bioprinter (BioAssemblyBot 400) using Gage repeatability and reproducibility (R&R), one-sample *t*-tests, analysis of variance (ANOVA), *F*-tests, and independent-samples *t*-tests. We show that the retrofitted platform matches or exceeds the commercial system's repeatability and pore-scale accuracy at an 89.6% lower capital cost, establishing industrial-robot retrofitting as a viable pathway to accessible, multi-axis robotic bioprinting.

Table 1 positions the present platform against these and other reported systems along five dimensions relevant to bioprinting-specific hardware retrofits: manipulator degrees of freedom, whether the hardware and software are openly released, whether the system accepts conventional slicer-generated G-code without a custom toolchain, whether G-code-to-robot translation occurs in real time or as an offline pre-processing step, and what validation endpoint, if any, was reported.

2. Materials and methods

2.1. Robotic platform and work cell

The retrofit is built around an ABB IRB 120T six-axis industrial robotic arm (Switzerland) driven by an IRC5 Compact controller (Figure 1A and 1B), an industrial platform not originally intended for bioprinting. A dedicated print bed was designed and mounted on the robot's support cart to provide a fixed, repeatable coordinate reference (workobject) for printing (Figure 1C). The bed was raised 4.75 in. (12.065 cm) above the cart surface on four aluminum extrusion legs (two 4.75 in. [12.065 cm] and two 6 in. [15.24 cm] to account for unequal mounting-surface heights) so that the entire print area remained within the robot's reachable, singularity-free workspace. A 12 in. × 12 in. (30.48 × 30.48 cm) aluminum sheet was mounted on the extrusion legs to provide a rigid, flat base, topped with a 10 in. × 10 in. (25.4 × 25.4 cm) glass print surface secured using four custom 3D-printed polylactic acid (PLA) corner brackets. A workobject (wobjPlate) referencing this glass surface was defined in RAPID, completing the tool- and work-coordinate definitions needed for print execution.

The printhead retrofitted onto this arm is an in-house low-cost, open-source hybrid extrusion bioprinting nozzle designed for mounting on conventional FDM gantries.[25] That printhead includes a metal syringe holder with an embedded heating element and temperature sensor, mounted through a 3D-printed PLA bracket (Figure 2A). To mount this printhead on the robot, the base bracket was modified with a rectangular extension containing four M5 clearance holes, matching the M5-tapped end-effector mounting pattern of the IRB 120T, and the modified bracket was 3D printed in PLA to preserve the low-cost character of the system. A tool center point was defined in RAPID for the syringe tip so that all subsequent robot motion commands could be issued directly in tool coordinates (Figure 2B and 2C).

2.2. Extrusion control circuit

Material extrusion is driven pneumatically and gated by a solenoid valve; because the source printhead's extrusion logic was written for FDM firmware, a dedicated circuit was built so the IRC5 controller could switch the solenoid on and off in step with G-code extrusion commands (Figure 3).

The controller's XS16 rail supplies 24 V/0 V reference, which was wired to the XS15 digital-output power rail to energize the XS14 digital-output bank; port 1 of XS14 was assigned to a digital output (doFan) dedicated to solenoid

Table 1. Comparison of the present retrofit platform against prior robotic and open-source/low-cost bioprinting and G-code-translation systems reported in the literature

System	Application field	Reported print speed	Build volume/Part size	Workspace/Safety envelope
Yang *et al.*[15] (KUKA LBR iiwa, 7-DOF)	*In situ* surgical bioprinting (volumetric muscle loss)	Not reported	Not reported (planar toolpaths only)	800 mm reach; collaborative-rated arm (reduced guarding requirement)
Albrecht *et al.*[16] (ABB IRB 120, 6-DOF)	Soft-tissue biomedical (planar/angled surfaces)	Not reported	Not reported	580 mm reach; industrial (non-collaborative) arm, standard guarding required
Fortunato *et al.*,[17,18] IMAGObot (5-DOF)	*In situ* cranial/bone defect reconstruction	Not reported	Custom, defect-specific geometry; not reported as a general build volume	Desktop-scale open frame; reduced footprint, no industrial guarding reported
Shojaei Barjuei *et al.*[14] (UR5e, 6-DOF)	Complex/Vascular tissue constructs (freeform curved & tubular)	Not reported (embedded/support-bath printing)	Not reported	850 mm reach; collaborative-rated (cobot), minimal guarding
Vasques & Figueiredo,[13] Delta robot Óscar (3-DOF, parallel)	General-purpose/Educational (not demonstrated for bioprinting)	Not reported for a bioprinting application	Not reported for a bioprinting application	Compact desktop footprint; minimal guarding, but cannot reorient tool (3 translational DOF only)
DED/Multi-axis robotic AM, general[12]	Metal/Polymer directed energy deposition, large-format AM	Process-dependent; typically much higher deposition rate than extrusion bioprinting (not directly comparable)	Often > 1 m (large-format)	Full industrial robotic cell; guarding and, for laser/arc DED, fume extraction required
Proposed work (ABB IRB 120T, 6-DOF)	Acellular hydrogel scaffold fabrication (extrusion); future robotic bioprinting	453.1 s per 40×40 mm two-layer scaffold (7.9 scaffolds/hr) at current, unoptimized handshake settings	Demonstrated part: 40×40 mm scaffold; robot reach 580 mm (workspace substantially larger than printed part)	580 mm reach; industrial (non-collaborative) arm—standard guarding recommended, unlike the cobots used in other studies[14,16]

Abbreviations: AM: Additive manufacturing; DED: Directed energy deposition; DOF: Degree of freedom.

control. Because the solenoid draws current near the 0.5 A limit of the controller's digital-output rail, and de-energizing an inductive coil produces a back-electromotive force voltage spike that can damage controller electronics, the circuit uses a MOSFET transistor to switch the solenoid's ground path and a 1 A diode wired in flyback configuration in parallel with the coil to safely dissipate the induced spike each time doFan transitions from high to low.

2.3. Real-time G-code-to-RAPID translation pipeline

The core software contribution is a real-time pipeline that intercepts standard, Marlin-format G-code—produced by slicing an STL file in the free slicer CuraSlicer,[26] exactly as for a conventional FDM printer—and translates it into RAPID motion and input/output (I/O) commands on the fly, without an offline path-generation step. While OctoPrint, CuraSlicer, and Python are free/open-source components of the developed workflow, ABB RAPID is executed within the proprietary IRC5/RobotWare environment provided with the ABB robot controller. Therefore, our use of the term *open-source* refers specifically to the developed software workflow and released integration components, not the ABB controller environment itself. The pipeline runs (Figure 4) on a Raspberry Pi hosting OctoPrint (United Kingdom), an open-source, browser-based 3D-printer control server. Because OctoPrint communicates with 3D-printers over a serial connection, a paired virtual serial port pair (/dev/ttyVIRTUAL, /dev/ttyEXT) was created on the Pi, and a lightweight Python program (fake_firmware.py) was written to emulate a 3D-printer's firmware responses on that channel—for example, returning an "ok" acknowledgment for temperature or handshake queries—so that OctoPrint would treat the connection as a normal printer and not time out (Figure 4).

A custom OctoPrint plugin (RobotSync), written in Python, hooks into OctoPrint's G-code sending queue

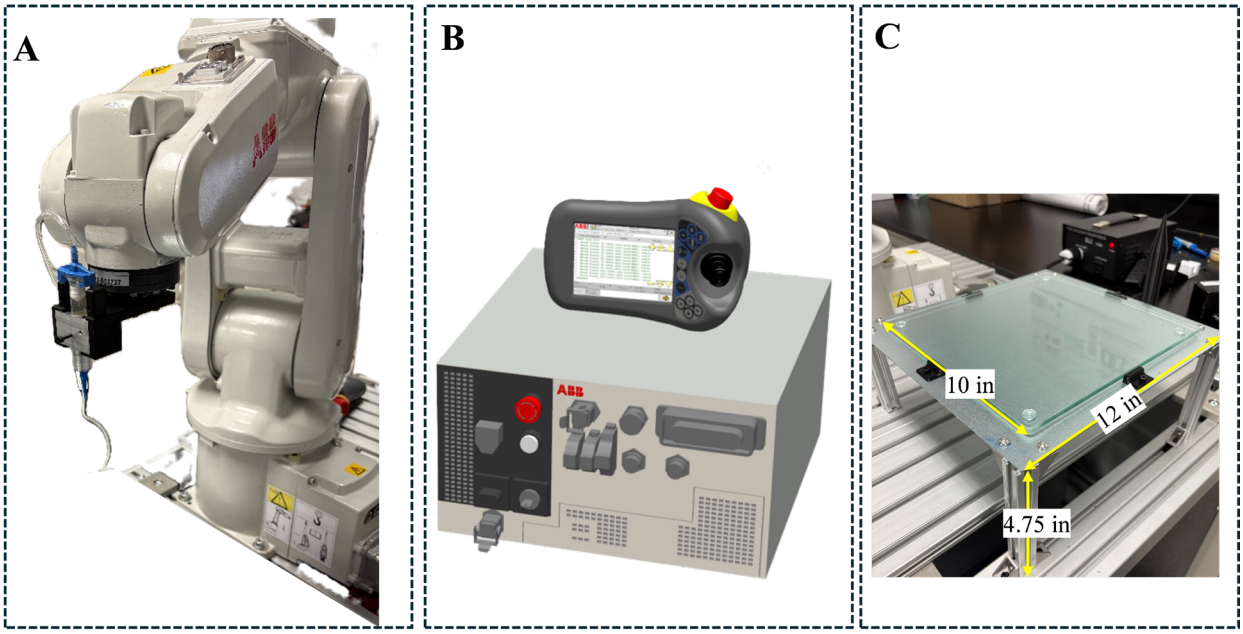


Figure 1. Hardware of the retrofitted robotic extrusion printing platform. (A) ABB IRB 120T six-axis industrial robotic arm with (B) IRC5 Compact controller, the retrofit platform used in this study, and (C) elevated glass print bed.

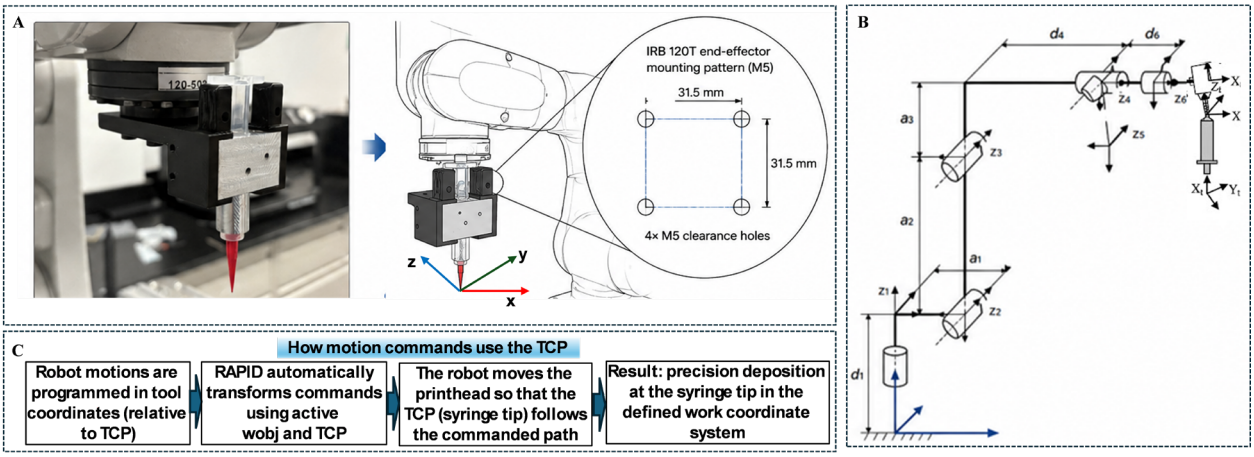


Figure 2. Printhead integration and tool-coordinate definition on the ABB IRB 120T. (A) Integration of the custom syringe-based printhead with the ABB IRB 120T, illustrating the modified mounting bracket. (B) Definition of the tool center point (TCP) at the syringe tip within the robot kinematic model. (C) The RAPID-based tool-coordinate framework that enables all motion commands to be executed relative to the TCP for precise material deposition.

and inspects every outgoing line. Coordinate-motion commands (G0, G1), dwell commands (G4), and positioning-mode commands (G90/G91) were intercepted before reaching the virtual serial port. In addition, the standard Marlin fan-control commands (M106/M107), which were repurposed in our custom OctoPrint implementation[24,25] to actuate the pneumatic extrusion system, were also intercepted, whereas all other commands were passed through with an immediate ok response. Communication between the Raspberry Pi and the IRC5 controller runs over a dedicated Ethernet link using TCP/IP socket commands native to RAPID (e.g., SocketCreate, SocketAccept), avoiding the serial expansion board that would otherwise be required and that would have added cost to the system.

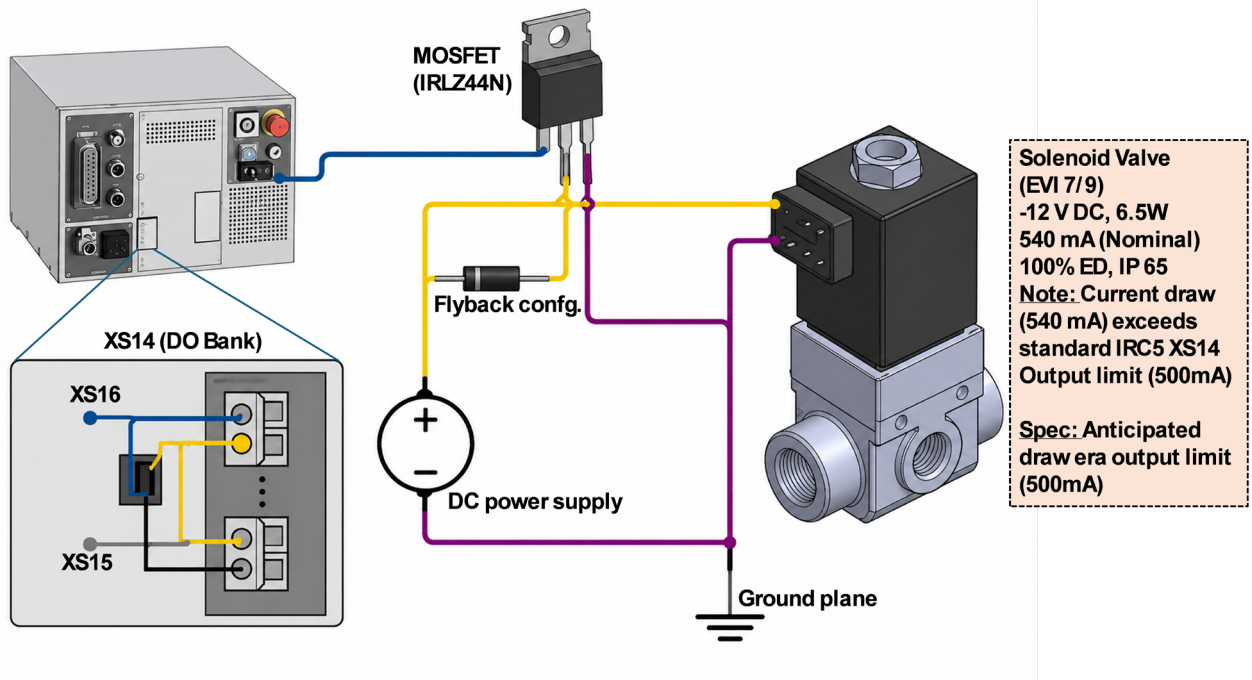


Figure 3. Solenoid extrusion-control circuit diagram. The IRC5 controller's digital output (doFan) switches a MOSFET, which gates the solenoid valve; a flyback diode protects the controller from inductive voltage spikes on de-energization.
Abbreviations: confg: Configuration; DC: Direct current; DO: Digital output; ED: Duty cycle (from German *Einschaltdauer* [energization duration]); IP: Ingress protection; Spec: Specification.

Execution is managed through a static G-code file hosted directly on the Raspberry Pi, which OctoPrint transmits line by line via the virtual serial port (Figure 5). To maintain precise real-time synchronization, intercepted movement and execution commands (*G*0, *G*1, *G*4, and *M*106/*M*107) pass through a two-stage handshake ensuring the robot never receives a new motion target while executing the previous instruction. In Stage 1, the plugin strips the extruder parameter (*E*) from movement commands, forwards the refined command string to the IRC5 controller, and waits for an OK acknowledgment once the RAPID program parses and buffers the target. Stage 2 subsequently issues an EXECUTE signal, holding OctoPrint until the motion or dwell cycle completes. In contrast, state-configuration commands (such as absolute *G*90 and relative *G*91 positioning modes) bypass the second handshake stage entirely; because they require no trajectory generation or runtime execution sync, they are identified and processed immediately in Stage 1. All unhandled or auxiliary commands bypass the handshake pipeline completely, passing directly through the virtual serial interface without synchronization overhead.

In stage 2, the plugin sends an EXECUTE signal; the RAPID program performs the buffered motion or I/O action and returns an EXECUTED signal once complete, at which point the plugin's block on OctoPrint's sending thread is released, and the next line may be sent. A daemon thread manages the EXECUTED wait with a 60 s timeout so that a stalled connection cannot hang the print indefinitely; the 5 s timeout used for the initial OK handshake reflects the much shorter time a parse-and-buffer step is expected to take.

On the controller side, the RAPID module parses each buffered command using four purpose-built routines. ExtractSpeed locates the feedrate parameter (F) and converts it from the Marlin standard of millimeters per minute to the RAPID standard of millimeters per second (division by 60), assigning the result to the active speeddata variable. ExtractCoords scans the remaining string character by character for X-, Y-, and Z-axis labels, extracts the associated numeric values into a coordinate array, and sets per-axis boolean flags marking which axes were updated in that command. GenerateTarget then builds the robtarget: under absolute positioning (G90) the parsed values are assigned directly, while under relative positioning (G91) the parsed values are added to the robot's last commanded position for only the flagged axes. Finally, the Execute routine dispatches the motion: G0 (rapid positioning) is executed as a joint move (MoveJ) and G1 (linear interpolation) as a linear move

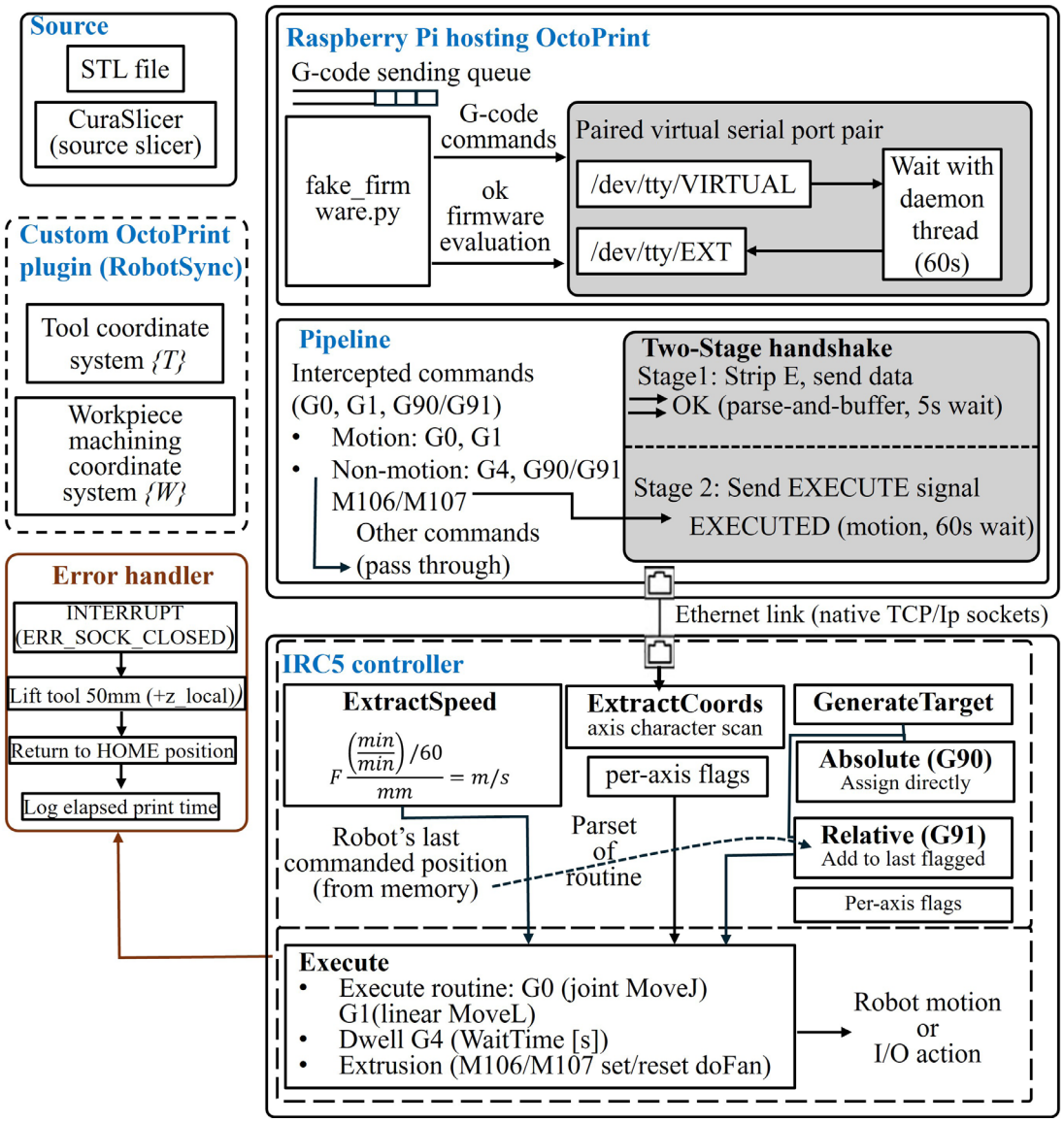


Figure 4. Block diagram of the real-time software pipeline executing on a Raspberry Pi to intercept Marlin G-code from OctoPrint, process it via a two-stage handshake, and transmit parsed motion and input/output (I/O) commands over Ethernet to an ABB IRC5 controller for native RAPID execution and error handling

(MoveL), while G4 dwell commands are converted from milliseconds to seconds, where required, and executed as a WaitTime pause. Pneumatic extrusion on/off commands (M106/M107) directly set or reset the doFan digital output described in Section 2.2. If the socket connection is interrupted mid-print (ERR_SOCK_CLOSED) or times out after 5 min of inactivity (ERR_SOCK_TIMEOUT), an automated error handler initiates a safety routine: it lifts the tool 50 mm along the local Z-axis to clear the workpiece, returns the robot to its predefined home position, and logs the elapsed print time in seconds via an onboard clock. Notably, because OctoPrint intentionally closes the socket upon job completion, an ERR_SOCK_CLOSED condition is also triggered naturally at the end of a successful print. Consequently, this same retraction, homing, and time-logging sequence double-functions as the standard end-of-print execution routine, recording the final total print duration.

2.4. Command mapping and coordinate handling

This section describes, at the implementation level, how intercepted G-code parameters were converted into RAPID

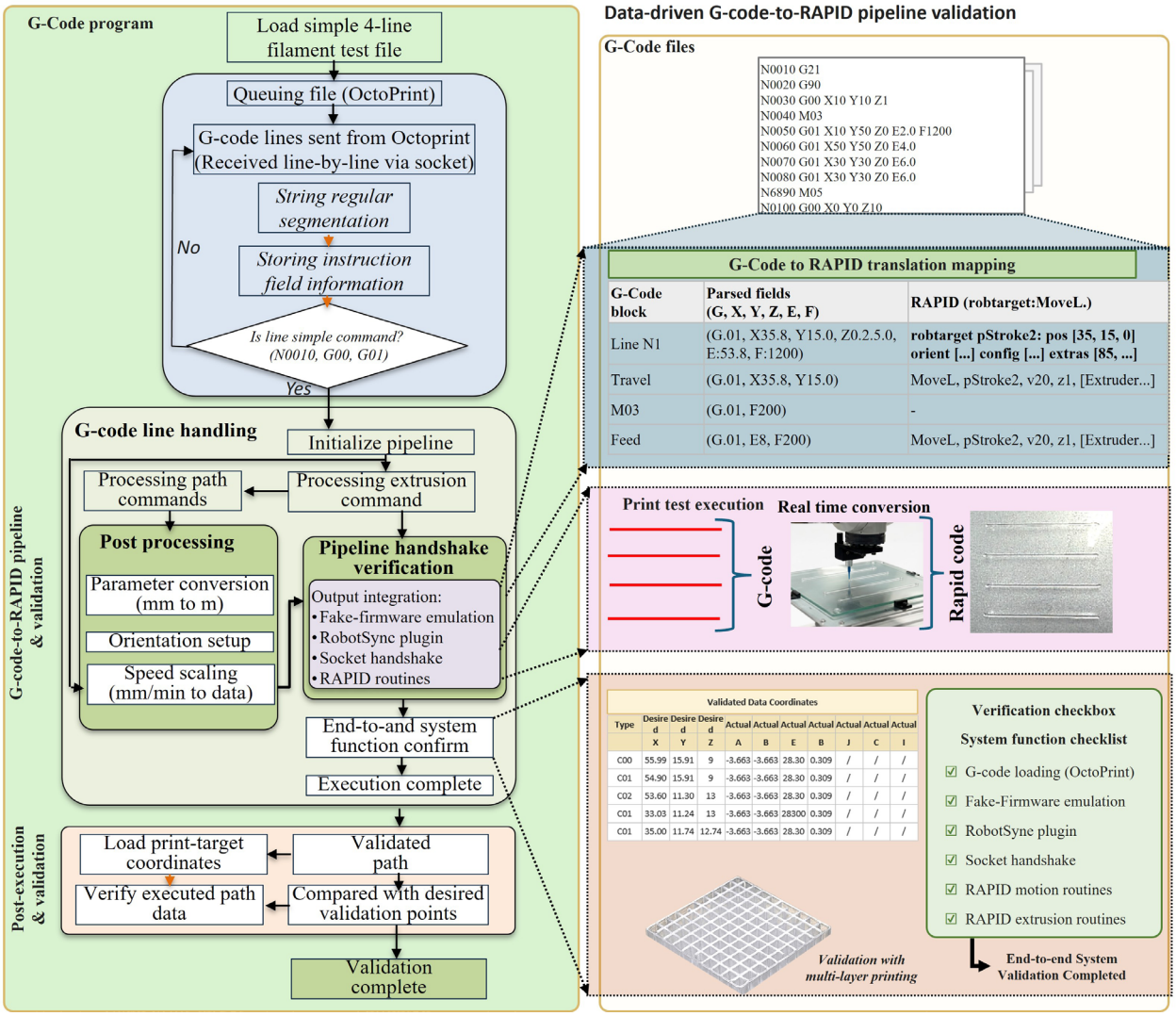


Figure 5. This system architecture diagram illustrates the comprehensive, multi-stage workflow of the data-driven G-code-to-RAPID pipeline, showcasing real-time toolpath post-processing, communication handshake verification via plugin emulation, and end-to-end experimental validation on an automated multi-axis printing system

motion and I/O commands. The retrofitted system does not solve inverse kinematics in software; the ABB IRC5 controller natively resolves joint-space motion whenever a MoveJ or MoveL instruction is issued to a target expressed relative to the predefined tool center point and workobject (Section 2.1). Feed rate values (F) parsed from incoming G-code, expressed in the Marlin convention of millimeters per minute, were converted to the RAPID convention of millimeters per second according to **Equation 1**:

$$v = \frac{F}{60} \tag{1}$$

where v is the resulting RAPID speed value assigned to the buffered target.

Target coordinates were generated according to the active positioning mode. Under absolute positioning (G90), each parsed axis value was assigned directly to the corresponding coordinate of the next robtarget. Under relative positioning (G91), only the axes flagged as present in the incoming command line were updated relative to the robot's last commanded position, according to **Equation 2**:

$$p_i = c_i \quad (\text{G90,absolute}) \quad \text{or}$$
$$p_i = p_{\text{last},i} + \Delta c_i \quad (\text{G91,relative}), \quad \text{for } i \in \{X, Y, Z\} \tag{2}$$

where c_i is the coordinate value parsed from the G-code line and $P_{\text{last},i}$ is the axis value from the previously issued target.

The resulting target was dispatched according to the primary G-code command identifier: G0 was executed as a joint move (MoveJ), G1 as a linear move (MoveL), and G4 as a timed pause (WaitTime) after unit conversion from milliseconds to seconds. Pneumatic extrusion on/off commands (M106/M107) directly set or reset the digital output (doFan) described in Section 2.2. Circular interpolation (G02/G03) was not exercised in the present validation experiments and is not claimed as part of the validated workflow.

2.5. Bioink, print geometry, and process parameters

All prints used our in-house acellular hydrogel bioink formulated from 4% (w/v) sodium alginate and 4% (w/v) carboxymethylcellulose (A4C4) in phosphate-buffered saline—a shear-thinning formulation widely used in extrusion bioprinting for its combination of flow behavior and post-deposition shape fidelity, and the formulation for which the source printhead was originally characterized.[27,28] The validation part was a lattice scaffold with a nominal design geometry of 40 × 40 mm containing 144 pores of nominal 3 × 3 mm; the sliced STL geometry actually used for metrology (after slicer-level wall/infill generation) had a nominal overall length/width of 41.21 mm and a nominal pore dimension of 3.43 mm (Figure 6), and these STL-derived values, not the nominal CAD design values, were used as the accuracy reference throughout.

On the retrofitted platform, A_4C_4 was extruded at room temperature at 17 psi (117.2 kPa), with no ionic or photo-induced crosslinking applied during or after printing. This pressure is higher than the 14 psi (96.53 kPa) at which A_4C_4 is nominally extruded; over-extrusion at 17 psi (117.2 kPa) was required within the project timeline to obtain continuous, gap-free strand deposition, and the resulting process condition—over-extrusion of an uncrosslinked, highly fluid hydrogel—is treated explicitly in Section 4 as a material/process-parameter characterization issue rather than a limitation of the robotic motion system. The commercial benchmark (BioAssemblyBot 400, Advanced Solutions Life Sciences; United States of America [USA]; hereafter, BioBot) was likewise run under a mild over-

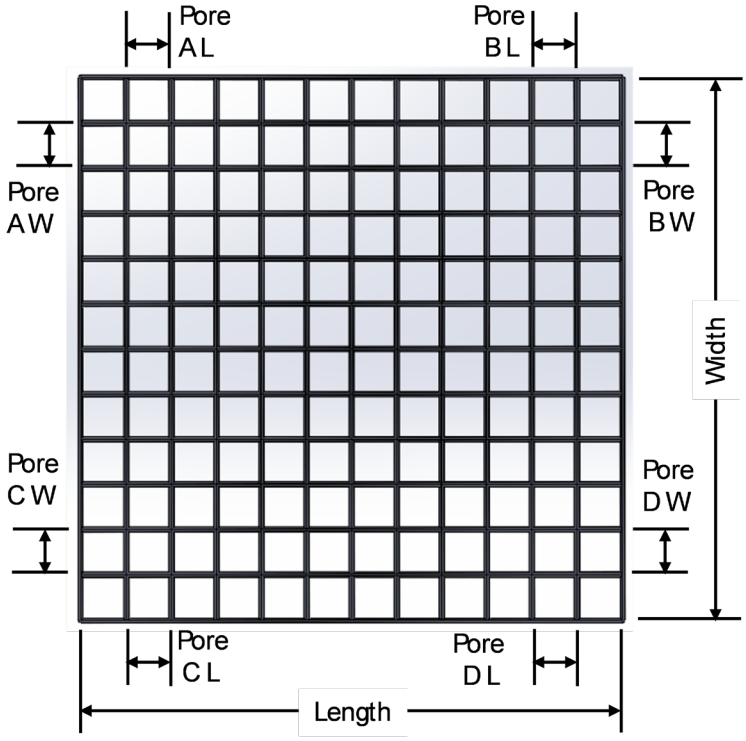


Figure 6. Target scaffold geometry: 144-pore lattice pattern used for all dimensional accuracy and repeatability testing (STL-derived overall dimension 41.21 mm; nominal pore dimension 3.43 mm). Pore L and Pore W represent pore length (L) and width (W), respectively, for individual pores at different locations.

extrusion condition, at 15 psi (103.42 kPa). Table 2 summarizes the bioink and process parameters for both platforms.

The "nozzle/needle gauge and standoff distance" row in Table 2 reports the nozzle inner diameter common to both platforms (0.7 mm); standoff distance was matched qualitatively through visual calibration on both systems but was not independently logged as a separate controlled numerical variable, and is not claimed to have been identical beyond that qualitative matching. Similarly, the "toolpath feedrate—deposition/travel" row reports a single toolpath speed (5 mm/s) used for both platforms; deposition and non-extruding travel moves were not commanded at separately logged speeds in this study. Layer height and the per-layer imaging delay were likewise not systematically varied or recorded for either platform. These unreported process variables are identified here as specific items to standardize and report in a future matched-benchmark comparison, rather than assuming they are identical on the basis of the values in Table 2 alone.

2.6. Print fabrication and metrology

Five scaffolds were printed on the retrofitted robotic platform and three on the BioBot for comparison. All prints were photographed with a Raspberry Pi HQ Camera Module (IMX477, Arducam, China) mounted at a fixed height of 4 in. (10.16 cm) above the print, with a digital caliper of known scale placed in-frame to allow pixel-to-metric calibration; physical (contact) measurement was not used because it would damage the uncrosslinked hydrogel. Images were imported into ImageJ (National Institutes of Health, USA), an open-source scientific image-analysis program, and the in-frame caliper was used to calibrate the pixel scale for each image. Ten features were measured on each scaffold: overall length, overall width, and the interior length and width of four pores (designated A–D) located in different quadrants of the lattice, so that any position-dependent bias could be detected. Each of the 10 features was measured three times by a single operator, and the mean of the three replicate measurements was used as that feature's recorded value for all subsequent analysis; the replicate measurements additionally supported the Gage R&R analysis. Because the printed BioBot scaffold lacked an outer perimeter wall present in the retrofitted-platform prints, the BioBot's overall length and width were additionally reported with a wall-thickness correction: the width of five individual strands was measured on each

Table 2. Bioink formulation, printing parameters, and validation scaffold geometry

Parameter	Retrofitted platform	BioBot (commercial)
Bioink	A_4C_4 (4% w/v alginate, 4% w/v carboxymethylcellulose, PBS)	Same (A_4C_4), identical batch/formulation
Cell content	Acellular	Acellular
Nominal A_4C_4 extrusion pressure (typical setpoint)	14 psi (96.53 kPa)	14 psi (96.53 kPa)
Actual extrusion pressure used in this study	17 psi (117.2 kPa; mild over-extrusion)	15 psi (103.42 kPa; mild over-extrusion)
Crosslinking (ionic or photo)	None applied	None applied
Printing temperature	Room temperature	Room temperature
Nozzle/Needle gauge and standoff distance	0.7 mm	0.7 mm
Toolpath feedrate—deposition/travel	5 mm/s	5 mm/s
Scaffold dimensions (CAD)	40 × 40 mm	40 × 40 mm
Number of pores	144	144
Nominal pore size (CAD)	3 × 3 mm	3 × 3 mm
Baseline scaffold dimensions (STL, used as accuracy reference)	41.21 × 41.21 mm	41.21 × 41.21 mm
Baseline pore size (STL, used as accuracy reference)	3.43 mm	3.43 mm

Abbreviations: CAD: Computer-aided design; PBS: Phosphate-buffered saline.

of the three BioBot prints, and the resulting mean strand width (0.964 mm; SD = 0.165 mm across the 15 individual strand measurements, reflecting print-to-print and strand-to-strand variability in the correction itself) was added to each raw overall-dimension measurement to place the two platforms' overall-dimension measurements on a comparable basis.

To evaluate multi-run process repeatability independently of absolute scale variations between macro-framework and micro-structural infill characteristics, all dimensional parameters were normalized. The relative percent deviation ($D_{i,j}$) for a given feature i in print run j from its respective collective experimental mean (μ_i) was defined according to **Equations 3** and **4**:

$$D_{i,j} = \left(\frac{x_{i,j} - \mu_i}{\mu_i} \right) \times 100 \quad (3)$$

$$\mu_i = \frac{1}{N} \sum_{j=1}^{N} x_{i,j} \quad (4)$$

where $x_{i,j}$ is the raw measured dimension of the feature, and μ_i is the average value computed across all five independent experimental runs. This dimensionless transformation yields a scale-invariant measure of each feature's run-to-run dispersion around its own experimental mean; it quantifies print-to-print precision, not accuracy relative to the STL target (which is addressed separately via the one-sample *t*-tests in Section 3.2), and reflects the combined influence of robot motion, print-to-print process variation, and measurement/image-analysis variance rather than an isolated measure of kinematic variance alone.

2.7. Statistical analysis

All measurements were compiled in Microsoft Excel (Microsoft Corporation, USA) and analyzed in Minitab 22 (Minitab, LLC, USA). A single-operator repeatability study was conducted using triplicate measurements of 10 distinct features to assess measurement-system precision on the retrofitted platform. Because all measurements were performed by a single operator across multiple features, the analysis evaluates measurement repeatability but does not assess operator-to-operator reproducibility. Descriptive statistics (mean, SD, coefficient of variation [CV], and range) were computed for both platforms. One-sample *t*-tests compared each measured feature's mean against its STL-derived target dimension to test for systematic deviation. A multi-way ANOVA ($\alpha = 0.05$) was performed on the retrofitted platform's dataset with print-run number (blocking factor), deposition direction (X/length vs. Y/width), and dimension class (overall vs. pore) as factors, including the direction × dimension-class interaction term. Finally, the two platforms were compared directly: *F*-tests evaluated whether dimensional variance (repeatability) differed between platforms, and independent-samples *t*-tests (with unequal variances assumed, consistent with the *F*-test results) evaluated whether mean dimensional accuracy differed between platforms. Both cross-platform tests were run separately for four feature groupings: overall dimensions, all pore dimensions pooled, pore dimensions in the X/length direction only, and pore dimensions in the Y/width direction only, because a consistent directional bias was observed in preliminary inspection of the raw data and warranted separate treatment.

F-tests for equality of variance are sensitive to departures from normality, particularly at the small per-platform sample sizes used here (five retrofitted prints vs. three BioBot prints); a Levene or Brown–Forsythe test would be a more robust alternative for future work with larger sample sizes. Meanwhile, because 10 features were measured per scaffold, the between-platform inferential tests pool multiple within-scaffold features; the printed scaffold, not the individual pore or repeated image measurement, is the conceptually appropriate experimental unit, and future studies should confirm these findings using scaffold-level or mixed-effects models with larger print counts. For each of the four feature groupings—overall dimensions, pooled pore dimensions, pore length in the X-direction, and pore width in the Y-direction—the relevant measurements were averaged within each printed scaffold to obtain a single independent value per scaffold. *F*-tests and independent-samples Welch's *t*-tests were then performed using the scaffold-level measurements ($n = 5$ for the retrofitted platform and $n = 3$ for the BioBot). The scaffold-level analysis is presented in Section 3.4 alongside the pooled analysis, with scaffold-level results as the primary comparison because each independently printed scaffold represents the experimental unit. A mixed-effects modeling approach that accounts for repeated pore measurements nested within individual scaffolds, combined with a larger number of independent prints per platform, could provide a more comprehensive statistical assessment in future validation studies. The four feature groupings tested at the scaffold level (eight tests total: four *F*-tests, four Welch's *t*-tests) were not corrected for multiple comparisons in the primary presentation above; a Holm–Bonferroni-adjusted analysis is reported alongside the raw results in Section 3.4, and the scaffold-level comparisons are best interpreted as exploratory, directional evidence at this sample size ($n = 5$ vs. $n = 3$) rather than confirmatory hypothesis tests.

3. Results

3.1. System functionality verification

Following assembly of the work cell and the G-code-

to-RAPID pipeline, a simple four-line filament print was executed to confirm end-to-end system function before formal validation testing began. OctoPrint queued the corresponding G-code, and the retrofitted platform completed the print without communication errors, confirming that the fake-firmware emulation, the RobotSync plugin, the socket handshake, and the RAPID motion/extrusion routines functioned together as intended. With basic functionality confirmed, formal dimensional validation testing was carried out.

3.2. Dimensional accuracy and repeatability of the retrofitted platform

Five 40 × 40 mm lattice scaffolds were printed on the retrofitted platform and photographed for ImageJ measurement (Figure 8A). To validate the long-term operational stability and repeatability of the custom real-time translation pipeline across discrete execution blocks, a relative process-deviation profile was constructed (Figure 8B). Given the substantial scale discrepancy between the macro-scale overall framework geometry (~39.5 mm) and the micro-scale localized infill features (~2.6 mm), plotting absolute dimensional errors would obscure micro-structural variance. Consequently, dimensional parameters across five independent consecutive print runs were normalized as a percentage deviation from their collective experimental mean, yielding a scale-invariant metric of system precision.

3.2.1. Multi-run process repeatability and scale-invariant geometric reliability

As demonstrated by the polar coordinate distribution in Figure 8B, the system exhibited consistent run-to-run reproducibility, characterized by highly concentric, tightly bound profiles across all five manufacturing cycles.

A key finding is the high structural constancy at the macro-scale; both the overall length and width axes demonstrated a nearly perfect overlay along the 0% deviation boundary, with maximum deviations constrained to less than ±0.5% (Figure 7). This tight grouping confirms that the virtual firmware emulation and the physical TCP/IP socket buffer operate with dimensional consistency compatible with deterministic execution timing. Per-command communication latency, jitter, and command rate were not independently measured in this study (Section 4.5); this inference is therefore drawn from the resulting print dimensions rather than from direct timing measurements, and a contribution from packet jitter or

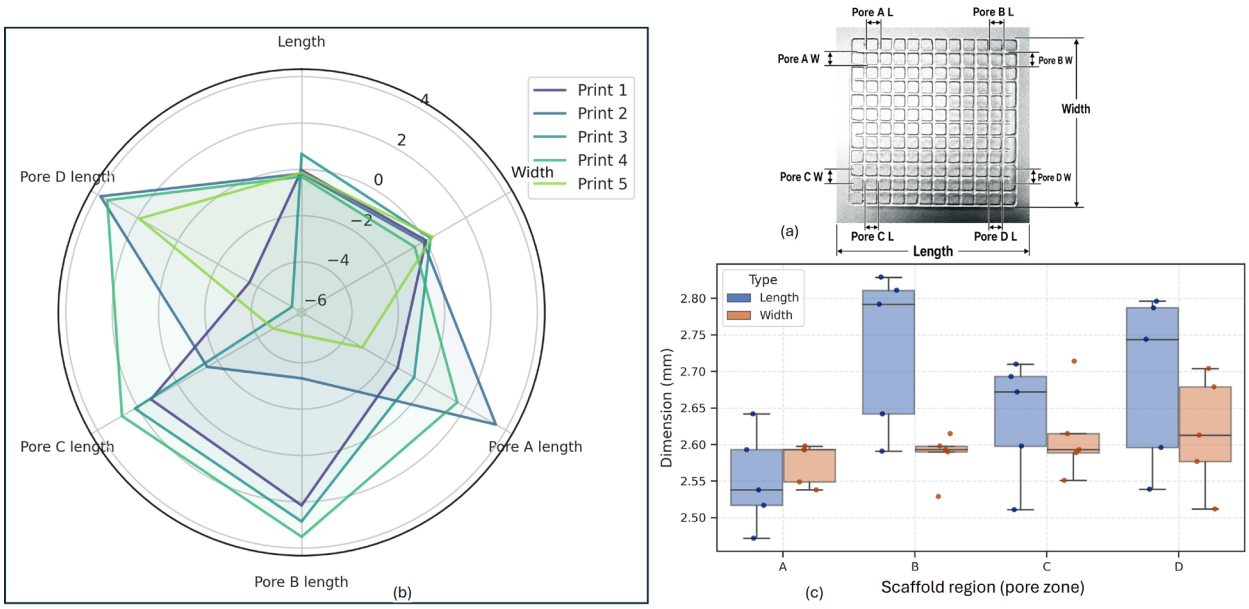


Figure 7. Dimensional evaluation of printed scaffold pores across multiple print runs. (A) Measurement locations for pore length (L) and width (W) at four scaffold regions (A–D). (B) Radar plot comparing pore dimension deviations across five print runs. (C) Box-and-whisker plots summarizing pore length and width distributions for each region, demonstrating dimensional fidelity, spatial variation, and print-to-print repeatability.

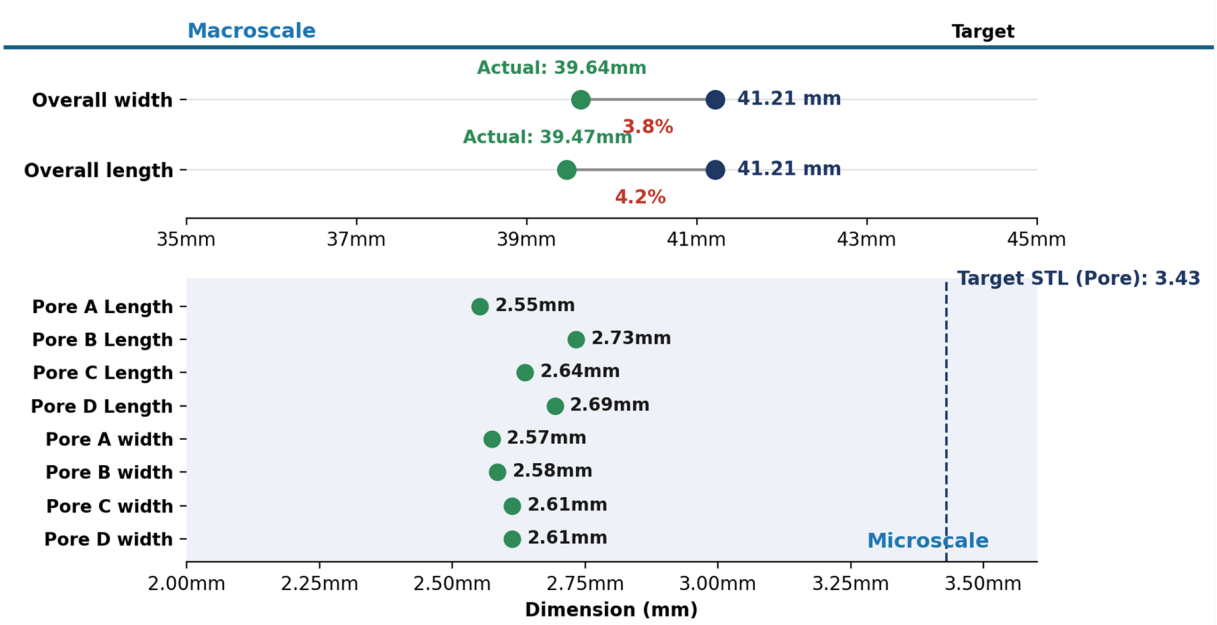


Figure 8. Comparison of target and measured scaffold dimensions for the retrofitted platform: target (STL) and experimentally measured dimensions for the overall scaffold and pore features, with percentage errors matching those reported in the surrounding text

cumulative transmission lag to macro-scale dimensional drift cannot be fully excluded by the present data alone.

Conversely, the micro-structural features (Pore A length through Pore D length) exhibited a slightly broader, yet highly systematic, distribution profile ranging from −6% to +4%. This localized variation highlights a distinct behavioral demarcation between global continuous extrusion paths and fine-pitch infill transitions. The narrowest deviation envelope among the micro-features was observed along the length and width vectors positioned near the top vertex of the radar chart, which correspond to long, uninterrupted linear path segments where the robot maintains steady-state velocity profiles.

In contrast, the broader dispersion profiles noted at the lower vertices (Pore B length and Pore C length) reveal the physical influence of localized kinematic constraints. Because individual pore boundaries require high-frequency execution of sharp-corner turnarounds, these regions were subject to transient velocity blending, structural deceleration phases, and small variations in dynamic motor torque response on the robot arm. The resulting minor fluctuations in instantaneous material shear rate manifest as localized path-width variations between successive runs. Despite these micro-scale dynamics, the maximum absolute deviation across all features remained tightly bounded within a narrow +6% window.

The localized distribution profiles of internal pore structures across distinct geographical regions (Zones A–D) were evaluated via a combined boxplot and jittered swarm analysis (Figure 8C). This spatial mapping isolates absolute dimensional variance while differentiating between the toolpath vectors corresponding to pore length and pore width. The system demonstrated consistent dimensional containment, with the majority of micro-features remaining tightly bounded within a narrow 2.50 mm to 2.70 mm window. Notably, the pore width vector displayed superior stability across all four zones—as highlighted by the highly compressed box profiles in Zones B and C—confirming highly consistent track pitch spacing and deterministic steady-state material flow. Conversely, a marginal directional anisotropy was observed in the length measurements of Zones B and D, which exhibit elongated box limits and wider data-point dispersion. This axis-specific deviation does not indicate a system error; rather, it reflects the mechanical realities of continuous toolpath transitions. The high geometric uniformity and lack of severe, asymmetric profile distortion across the five test iterations provide evidence, within the scope of this five-print dataset, that the integrated pipeline translates standard G-code commands into stable, structurally predictable, uniform physical parts.

3.2.2. Global fidelity and scale-dependent manufacturing error profiling

To characterize the baseline translation accuracy of the integrated pipeline, a multi-scale dimensional comparison was performed between the nominal CAD/STL targets and the resulting physical prints (Figure 9). A clear, scale-dependent behavioral split was observed between macro-structural boundaries and localized micro-features. At the macro scale, overall boundary dimensions exhibited high fidelity to the nominal CAD geometries; the absolute mean deviations for length and width were restricted to −1.738 mm and −1.573 mm, respectively, translating to tight relative error rates of only −4.22% and −3.82% (Figure 8, right panel). This demonstrates that long continuous multi-axis toolpaths maintain excellent global geometric constraint.

Conversely, the micro-scale internal geometries presented a systematically amplified relative error profile, with all localized pore dimensions exhibiting negative deviations ranging from −20.32% to −25.59%. As isolated in Figure 8, the nominal 3.43 mm pore targets uniformly contract to an actual printed range between 2.55 mm and 2.73 mm. This structural under-dimensioning is highly uniform across both the length and width axes of all four quadrants (Pore A–D), indicating that the error is not an artifact of directional toolpath skewing or axis-binding.

The 3.43 mm STL-derived pore reference used throughout this study represents the sliced-model grid pitch (center-to-center pore spacing) rather than the strut-width-corrected clear pore opening. Twelve such pitches spanned 41.16 mm of the scaffold's 41.21 mm nominal width, indicating that the reference primarily reflects the tiled grid spacing rather than the clear opening after accounting for strut thickness. Because the same pitch-based reference was applied consistently to the CAD/STL model and printed constructs from both platforms, the reported percentage deviations provide an internally consistent basis for comparison. Nevertheless, a strut-width-corrected clear-opening reference, explicitly distinguished from the grid pitch, would provide a more rigorous measure of absolute dimensional accuracy and is therefore identified as an area for future refinement.

Instead, this consistent material contraction points to a combination of material-specific rheological behavior (e.g., viscoelastic die-swell adjustments during deposition) and the slicing software's internal calculation of toolpath

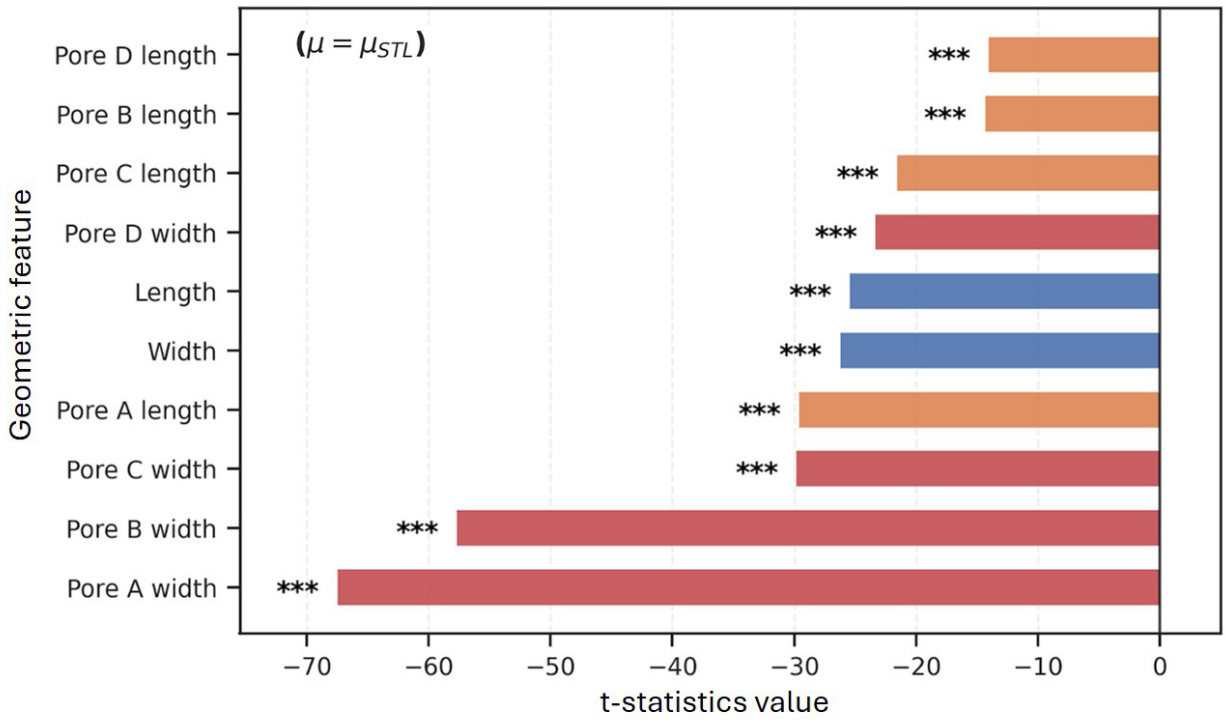


Figure 9. Statistical comparison of measured and target scaffold dimensions: One-sample *t*-test results comparing measured dimensions with the corresponding STL design values ($\mu = \mu_{STL}$). Negative *t*-statistics indicate dimensional shrinkage, while asterisks (***) denote statistically significant differences ($p < 0.001$).

centerlines for fine-pitch grids. Because the relative error was highly systematic and exhibited a narrow standard distribution across all micro-features, it can be mathematically countered with predictive pre-scaling factors in the G-code preprocessor, validating the overall deterministic reliability of the translation pipeline. Figure 8 presents the dimensional measurements of scaffolds fabricated using the retrofitted platform. The measured overall length and width were 39.472 mm and 39.637 mm, respectively, corresponding to dimensional deviations of −4.22% and −3.82% from the nominal values. Across the eight evaluated pore features, dimensional deviations ranged from −20.32% to −25.59%, indicating a consistent reduction in pore dimensions relative to the STL-derived reference. Collectively, these measurements characterize the dimensional accuracy of the retrofitted platform at both the overall scaffold and individual pore levels.

3.2.3. Statistical significance testing via one-sample t-test

To confirm whether the deviations from the intended design files represent statistically significant structural under-dimensioning rather than random measurement noise, a series of two-tailed one-sample *t*-tests were executed against the nominal CAD/STL baselines ($\mu_{printed} = \mu_{STL}$). The calculated statistical profiles are summarized in Figure 9. The analysis reveals that the null hypothesis ($\mu_{printed} = \mu_{STL}$) must be decisively rejected for every evaluated geometric parameter. All features yielded extremely high-magnitude negative *t*-values paired with critical significance values of $p < 0.001$. At the macro scale, global boundary constraints showed substantial divergence from nominal models (length: $t = -25.45$; width: $t = -26.22$). This statistical divergence became severely pronounced within localized microstructural elements, culminating in extreme significance parameters for Pore A width ($t = -67.46$) and Pore B width ($t = -57.67$). The massive scale of these negative *t*-statistics demonstrates that the systematic dimensional contraction observed across the scaffold grid is an exceptionally robust, non-random physical phenomenon. This confirms that geometric deviations are driven by highly reproducible processing variables—such as toolpath centerline interpolation or material thermal contraction— supporting predictive algorithmic pre-scaling within the translation preprocessor pipeline as a reasonable next step.

All 10 features were consistently undersized relative to the STL target, with a maximum absolute deviation of 1.81 mm (overall length). Overall-dimension accuracy—the printed mean expressed as a percentage of the STL target—was 95.78% for length and 96.18% for width; pore-dimension accuracy ranged from 75.69% to 77.37% of the target. One-sample *t*-tests confirmed that every feature's deviation from its STL target was statistically significant (all $p < 0.001$), consistent with a uniform, systematic undersizing rather than random print-to-print scatter.

Despite this systematic accuracy offset, repeatability was high: the maximum SD across all 10 features was 0.153 mm, the maximum range was 0.388 mm, and the mean CV across all features was 2.25%. The single-operator Gage R&R study (Table 3) returned study variation percentage and contribution percentage values above the conventional 30% threshold used to flag an inadequate measurement system for 8 of the 10 features. Read in isolation, this would suggest a measurement-system problem; read alongside the low CVs, it indicates that the physical variation between printed scaffolds was so small that the resolution limit of manual ImageJ landmark placement—not the printer—became the dominant source of the observed measurement variance. All 10 features returned a number of distinct categories of 1, meaning the measurement system, at this resolution, could not further subdivide print-to-print variation—the expected outcome once true part-to-part variation approaches the measurement system's own resolution floor, rather than an artifact of an unreliable gauge.

To express this repeatability in absolute terms: the pooled within-print repeatability SD (from the triplicate same-image landmark placements underlying Table 3) ranged from 0.054 mm to 0.151 mm across the 10 features (mean 0.083 mm), i.e., at or below the pixel-to-metric resolution of the imaging setup. Because these repeated measurements were taken from a single photograph of each scaffold, Table 3 characterizes operator/landmark-placement repeatability under fixed image, calibration, and camera-positioning conditions; it does not capture reproducibility across separate image acquisitions, caliper recalibrations, or camera repositioning, which were not independently varied in this study and are noted as a direction for future measurement-system validation.

3.3. Multi-way ANOVA and interaction dynamics

A multi-way ANOVA (Figure 10) was used to identify the dominant sources of dimensional variation in the retrofitted platform's prints. Print-run number, included as a blocking factor, was not statistically significant ($F = 0.46$, $p = 0.761$), indicating high run-to-run consistency and, by extension, reliable G-code parsing and execution across prints.

Deposition direction (X/length vs. Y/width) was likewise not significant ($F = 2.19$, $p = 0.146$), indicating that the robot's motion control did not introduce a directional kinematic bias of its own. Dimension class

Table 3. One-operator Gage R&R results for all 10 measured features on the retrofitted platform

Feature	Study variation percentage (%)	Contribution percentage (repeatability; %)	NDC
Length	77.00	59.29	1
Width	59.89	35.87	1
Pore A length	87.62	76.78	1
Pore B length	74.11	54.92	1
Pore C length	57.93	33.56	1
Pore D length	60.62	36.74	1
Pore A width	100.00	100.00	1
Pore B width	100.00	100.00	1
Pore C width	87.04	75.76	1
Pore D width	73.81	54.47	1

Abbreviations: NDC: Number of distinct categories; R&R: Repeatability and reproducibility

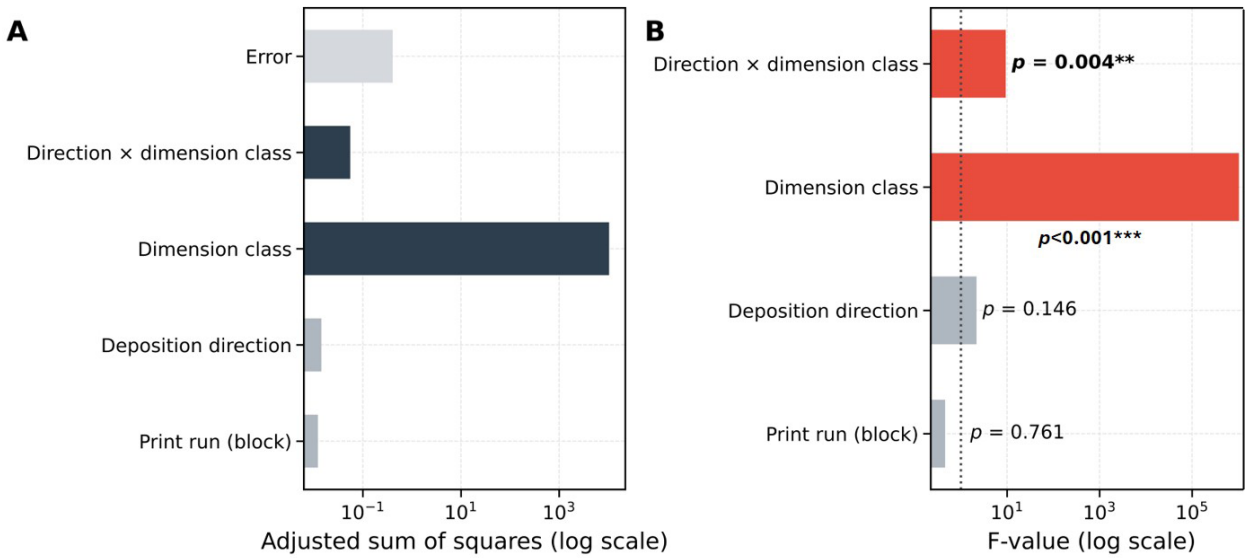


Figure 10. Contribution of process factors to dimensional error on the retrofitted platform. (A) Adjusted sum of squares showing the relative contribution of each factor to dimensional error. (B) Analysis of variance (ANOVA) *F*-statistics identifying significant effects, with dimension class and direction × dimension class exhibiting the strongest influence on scaffold dimensions.

(overall vs. pore) was highly significant (F = 1,036,182.01, $p < 0.001$), as expected given the large, deliberate difference in scale between overall and pore features, and is not itself evidence of a process problem. The direction × dimension-class interaction was also significant (F = 9.38, $p = 0.004$), indicating that the small directional effect present in the data depends on whether an overall or pore feature is being measured—consistent with a viscoelastic relaxation mechanism in which the first-deposited (X-direction) strands have more time to spread under gravity before the second layer (Y-direction) is deposited over them, before they have been crosslinked.

3.4. Comparative performance against the commercial BioBot

Three scaffolds were printed on the commercial BioAssemblyBot 400 (BioBot) under the same target geometry. Because the BioBot's printed scaffolds lacked the outer perimeter wall present in the retrofitted-platform prints, strand width was independently measured on five strands per print, and the resulting mean (0.964 mm) was added to the raw overall length and width measurements to place both platforms on a comparable basis (Figure 11).

The dimensional characterization of the bioprinted scaffolds demonstrated high reproducibility across three independent print runs, with consistent overall scaffold dimensions and pore geometries. The overall scaffold length and width exhibited low variability, with CVs of 1.01% and 1.56%, respectively, indicating excellent process repeatability. The radar plot revealed that while minor deviations existed among individual pore dimensions, the geometric distribution remained consistent across all print runs. Box plot analysis further showed that pore widths were generally more uniform than pore lengths, with Pores B and D exhibiting the lowest variability (CVs = 1.62%–4.15%), whereas Pores B and C lengths displayed relatively greater variation (CVs = 9.15%–10.62%). In addition, the aggregate strand width remained stable between print runs, with measured mean values of 0.952, 0.811, and 1.128 mm for Prints 1–3, respectively, confirming reliable filament deposition and overall geometric fidelity during robotic bioprinting.

To evaluate the fabrication performance of the proposed bioprinting platforms, a comparative analysis was performed linking qualitative CAD-to-print morphological deviations (Figure 12) directly with quantitative dimensional reproducibility (Figure 13).

The translation of the digital grid design (STL model) into physical scaffolds revealed distinct differences in toolpath tracking and material deposition behavior between the two printing systems (Figure 12). As illustrated by the schematic overlays in Figure 12D–F, the commercial baseline system exhibited characteristic extrusion-based defects, including pronounced corner rounding, localized over-deposition at junctions, and variable pore perimeter shrinkage. Conversely, the proposed system visually appeared to track the sharp transitions of the CAD nominal profile more closely, based on qualitative inspection of the overlays in Figure 12D–F rather than a registered-image quantitative contour-error metric; a quantitative contour-tracking analysis is identified as future work. The proposed system's prints maintained uniform strut widths and preserved the square cross-sections of the internal pore

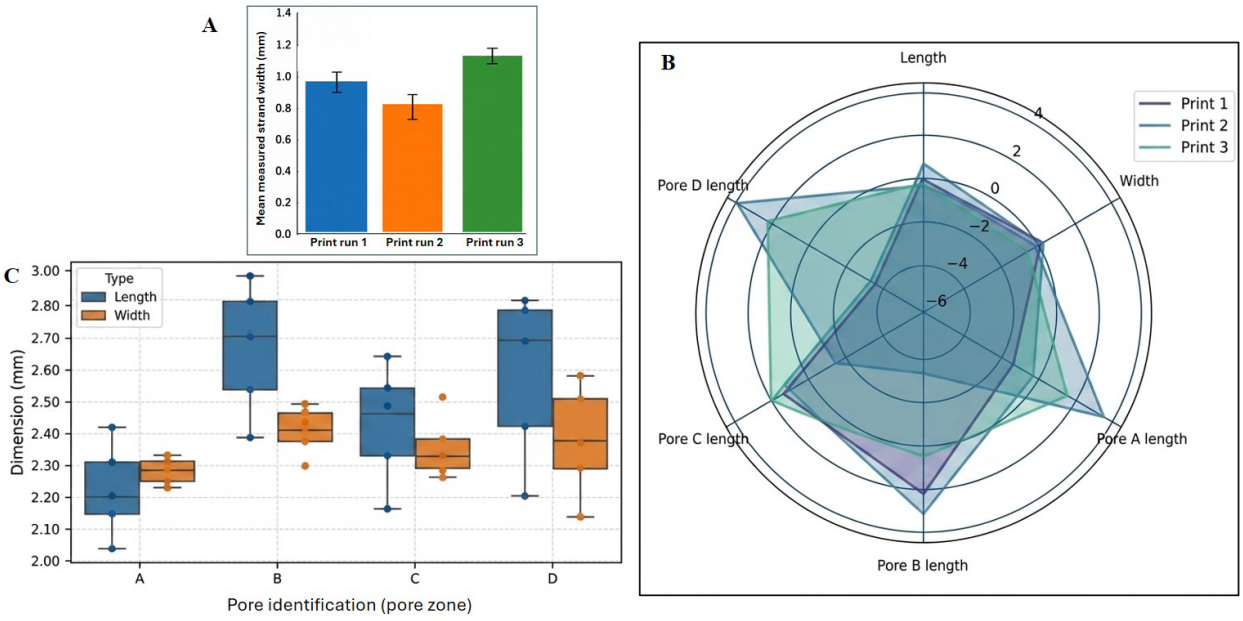


Figure 11. Dimensional fidelity and pore architecture evaluation for BioAssemblyBot 400 3D printing: (A) Mean measured strand width across three independent print runs (Print 1–3) showing process consistency and error margins. (B) Radar plot illustrating percentage dimensional deviations across macro dimensions (length, width) and internal pore lengths (Pores A–D). (C) Box plots detailing the spatial distribution and variance of internal pore dimensions (length and width) categorized by pore zone (A through D).

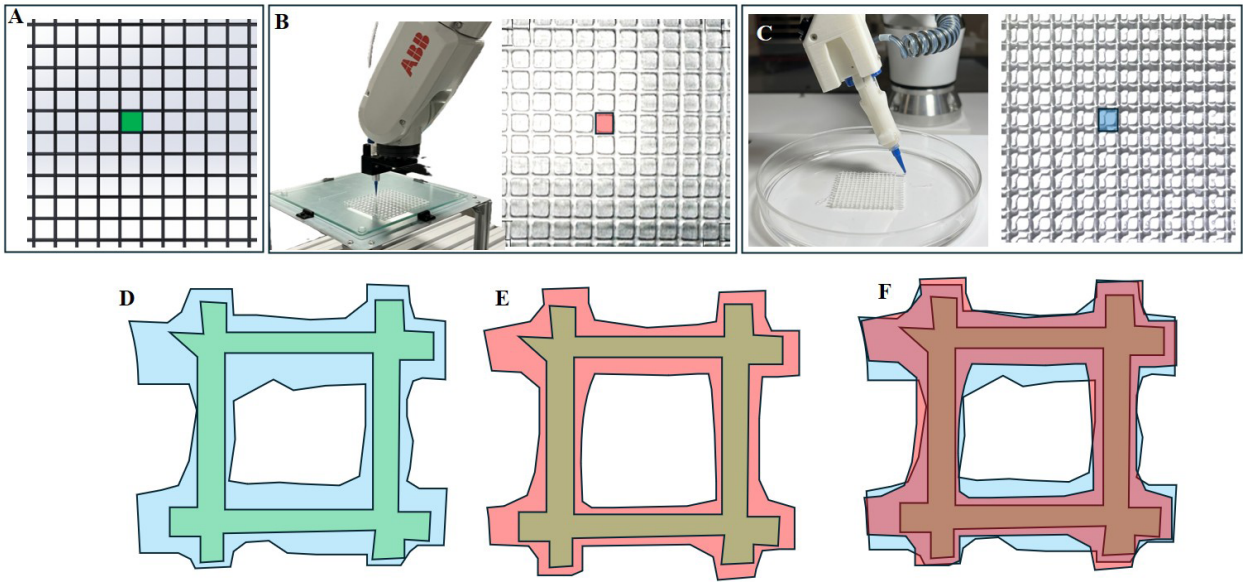


Figure 12. Comparison of scaffold geometry between the design model and printed constructs. (A) Target computer-aided design (CAD)/STL geometry. (B) Scaffold printed using the developed robot-assisted bioprinter. (C) Scaffold printed using the commercial BioAssemblyBot 400 bioprinter. (D) Overlay of the CAD model and BioAssemblyBot 400 print. (E) Overlay of the CAD model and robot-assisted print. (F) Composite overlay of the CAD model, robot-assisted print, and BioAssemblyBot 400 print, illustrating geometric agreement and dimensional deviations between the two printing platforms.

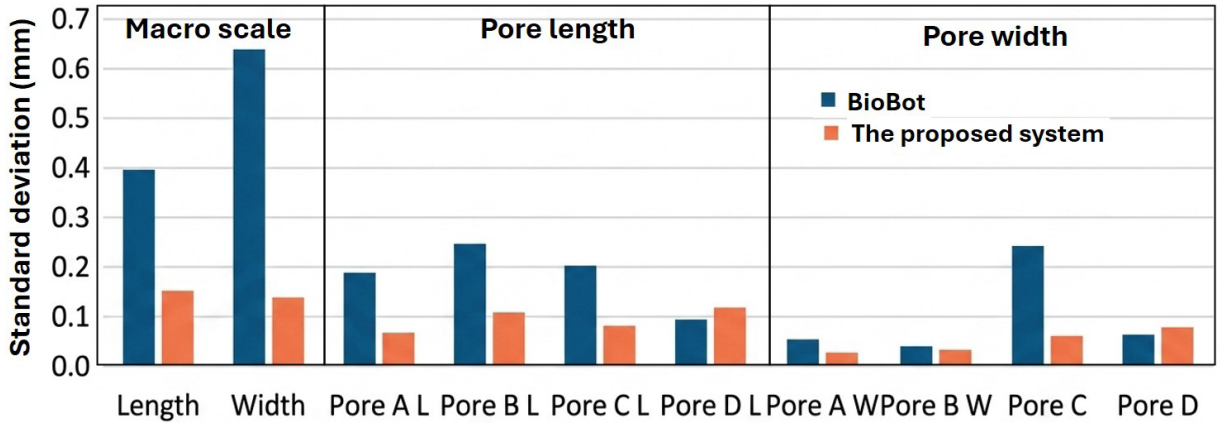


Figure 13. Dimensional variability comparison: SD (mm) of macro-scale features (length, width) and micro-scale pore features (pore length, pore width) for the BioBot baseline and the proposed system

zones (A through D).

To mathematically substantiate these visual improvements, print-to-print variability was quantified using the SD of key features across multiple prints (n = 5; Figure 13). High reproducibility is critical to ensuring uniform mechanical properties and predictable cellular infiltration behavior across fabricated cohorts.

The following results are obtained:

(i) Macro-scale dimensional stability: At the macro-scale, the visual tracking improvements of the proposed system translated into a substantial reduction in external boundary variance (Figure 13). The SD for scaffold width was reduced by over 78%, dropping from 0.638 mm in the BioBot baseline to 0.140 mm in the proposed system. Similarly, macro-scale length variation dropped from 0.399 mm to 0.150 mm. This confirms that the mechanical and kinematic upgrades

of the proposed system minimize bulk structural drift during layer-by-layer stacking.

(ii) Micro-scale pore reproducibility: This stabilized performance is mirrored at the micro-scale within the internal pore regions (Figure 13, pore length and pore width groups). The spatial deviations diagrammed in Figure 13 are reflected in the highly dispersed pore dimensions of the baseline prints. The proposed system mitigated this dispersion, reducing Pore A length variation from 0.190 mm to 0.068 mm (64.2% reduction) and Pore C width variation from 0.242 mm to 0.061 mm (74.8% reduction).

(iii) Localized variances: Only minor, localized fluctuations in variance were observed at the extreme boundaries, with the proposed system exhibiting marginally higher but comparable SDs restricted to Pore D length (0.120 mm vs. 0.095 mm) and Pore D width (0.078 mm vs. 0.063 mm).

By correlating the spatial CAD-conformance schematics (Figure 13) with the multi-scale variance distribution (Figure 14), we demonstrated that the proposed system suppressed the mechanical and fluid-dynamic fluctuations inherent to conventional extrusion setups, delivering the geometric reproducibility required for high-fidelity tissue scaffold manufacturing.

F-tests comparing dimensional variance between the two platforms were significant for all four feature groupings, indicating that the platforms' repeatability differs and is not attributable to chance. In every grouping, the BioBot showed the larger variance: across all 10 features, the retrofitted platform's mean SD was 0.087 mm vs. 0.217 mm for the BioBot (a 60% reduction), its mean CV was 2.25% vs. 5.07% (a 56% reduction), and its maximum dimensional range was 0.388 mm vs. 1.130 mm (a 66% reduction) (Figure 13). Independent-samples *t*-tests comparing mean accuracy reported no significant difference for overall dimensions ($t = -0.87$, df = 5, $p = 0.423$) or pore width in the Y-direction ($t = -1.33$, df = 12, $p = 0.210$)—i.e., no statistically significant difference in accuracy was detected on those features—but did report a significant difference for pore dimensions pooled ($t = -4.97$, df = 27, $p < 0.001$) and specifically in the X/length direction ($t = -7.14$, df = 16, $p < 0.001$). The retrofitted platform produced pore-length measurements that were significantly closer to the STL target than those obtained with the BioBot. To account for the independence of individual printed scaffolds, this comparison was further evaluated using scaffold-level analysis.

To account for the hierarchical structure of the measurements, the cross-platform comparison was repeated using individual scaffolds as the unit of analysis (Tables 4–6; $n = 5$ for the retrofitted platform and $n = 3$ for BioBot). This scaffold-level analysis modified the conclusions regarding repeatability but produced accuracy results consistent with those obtained from the pooled analysis. For repeatability, a significant difference in variance was observed only for the overall-dimension grouping ($F = 12.57$, $p = 0.038$), with the retrofitted platform exhibiting lower variability than BioBot (SD = 0.129 vs. 0.457 mm). Differences in variance were not statistically significant for pooled pore dimensions ($F = 2.17$, $p = 0.461$), pore length/X ($F = 8.70$, $p = 0.070$), or pore width/Y ($F = 2.92$, $p = 0.331$), although the retrofitted platform exhibited numerically lower variance across all feature groupings.

The scaffold-level accuracy analysis was consistent with the pooled analysis. The retrofitted platform demonstrated significantly greater accuracy for pooled pore dimensions (Welch's $t = 7.32$, df = 3.14, $p = 0.0045$) and pore length/X (Welch's $t = 4.20$, df = 2.28, $p = 0.041$). In contrast, no significant differences between platforms were observed for overall dimensions (Welch's $t = -2.26$, df = 2.19, $p = 0.141$) or pore width/Y (Welch's $t = 1.67$, df = 2.85, $p = 0.198$).

Collectively, the agreement between the pooled and scaffold-level analyses indicates that the conclusions regarding accuracy were robust to the choice of analytical unit. However, the repeatability advantage was statistically supported only at the macro-scale overall dimensions, while pore-scale measurements showed a numerically favorable but statistically nonsignificant trend toward lower variability for the retrofitted platform. Because the scaffold-level comparison included only three BioBot scaffolds, these analyses had limited statistical power. Accordingly, the scaffold-level results are presented as a more conservative comparison using the appropriate independent experimental unit, and the limited sample size should be considered when interpreting the pore-scale repeatability results.

3.5. Print speed, throughput, and cost

The BioBot completed each scaffold in a recorded 360.0 s, versus a mean of 453.1 s (robot clock)/449.8 s (OctoPrint clock) for the retrofitted platform. The retrofitted platform required 25.9% longer printing time per scaffold, corresponding to an hourly throughput of 7.9 scaffolds, compared with 10.0 scaffolds per hour for the BioBot. Thus, the retrofitted system exhibited a 20.6% lower hourly throughput, or equivalently, the commercial BioBot provided an approximately 26% throughput advantage. These values distinguish the increase in individual print duration (25.9%) from the corresponding decrease in

Table 4. Scaffold-level reanalysis of the cross-platform comparison, computed by first averaging within each scaffold to avoid pooling non-independent pore measurements

Grouping	Retrofit mean ± SD (mm; $n = 5$)	BioBot mean ± SD (mm; $n = 3$)	F-test (F, p)	Welch's t-test (t, df, p)
Overall dimension	39.554 ± 0.129	40.164 ± 0.457	$F = 12.57$, $p = 0.038$*	$t = -2.26$, df = 2.19, $p = 0.141$
Pore dimensions pooled	2.625 ± 0.033	2.392 ± 0.049	$F = 2.17$, $p = 0.461$	$t = 7.32$, df = 3.14, $p = 0.0045$*
Pore length, X-direction	2.654 ± 0.054	2.253 ± 0.160	$F = 8.70$, $p = 0.070$	$t = 4.20$, df = 2.28, $p = 0.041$*
Pore width, Y-direction	2.596 ± 0.037	2.530 ± 0.062	$F = 2.92$, $p = 0.331$	$t = 1.67$, df = 2.85, $p = 0.198$

Note: *$p < 0.05$.
Abbreviation: df: Degrees of freedom.

Table 5. Individual scaffold-level values underlying Table 4

Grouping	Retrofit individual scaffold values (mm; $n = 5$)	BioBot individual scaffold values (mm; $n = 3$)
Overall dimension	39.553, 39.497, 39.737, 39.387, 39.597	40.110, 39.737, 40.646
Pore dimensions pooled	2.595, 2.658, 2.616, 2.662, 2.594	2.448, 2.362, 2.365
Pore length, X-dir	2.644, 2.670, 2.645, 2.730, 2.579	2.437, 2.149, 2.174
Pore width, Y-dir	2.546, 2.647, 2.586, 2.593, 2.608	2.459, 2.576, 2.556

Note: One value per printed scaffold, averaged across that scaffold's own replicate pore/landmark measurements.

Table 6. Effect sizes, 95% confidence intervals (Welch–Satterthwaite), and Holm–Bonferroni-adjusted p-values for the four scaffold-level comparisons in Table 4

Grouping	Mean difference (retrofit – BioBot; mm [95% CI])	Hedges g	F-test raw p (Holm-adj. p)	Welch's t raw p (Holm-adj. p)
Overall dimension	−0.610 [−1.679, 0.459]	−1.868	0.038 (0.264)	0.141 (0.564)
Pore dimensions pooled	+0.233 [0.134, 0.332]	5.190	0.461 (0.461)	0.0045 (0.036)*
Pore length, X-direction	+0.401 [0.035, 0.766]	3.406	0.070 (0.350)	0.041 (0.248)
Pore width, Y-direction	+0.066 [−0.064, 0.196]	1.229	0.331 (0.662)	0.198 (0.595)

Notes: 8 tests total: 4 F-tests + 4 Welch's t-tests, corrected jointly. Mean differences and Hedges g are computed retrofit-minus-BioBot; a positive value indicates the retrofitted platform's mean was closer to the STL target (for the pore groupings) or larger (for overall dimension). Only the pooled pore-dimension accuracy comparison remains significant at $\alpha = 0.05$ after correction. *Holm-adjusted $p < 0.05$.

hourly throughput (20.6%). This speed deficit is consistent with the latency introduced by the two-stage software handshake described in Section 2.3, which pauses motion at every command boundary until an EXECUTED acknowledgment is received. This throughput gap is one of several respects in which the BioBot's purpose-built software stack remains more mature than the present retrofit: the commercial system ships with an integrated human–machine interface (HMI), a library of pre-validated toolpath patterns, and path-wise control over print speed and extrusion pressure, none of which the retrofitted platform currently replicates—the RobotSync

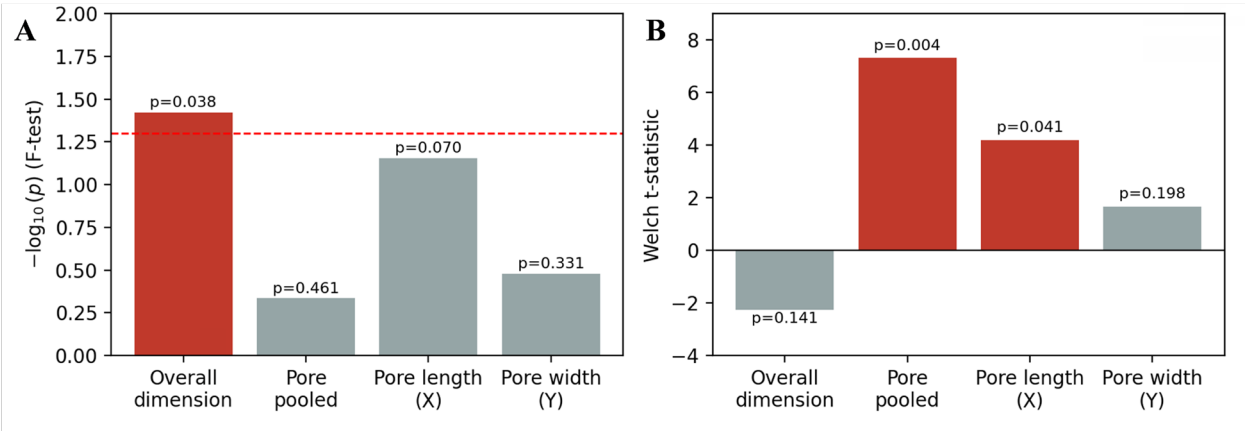


Figure 14. Scaffold-level statistical comparison between the retrofitted platform (n = 5) and BioBot (n = 3). (A) Repeatability comparison based on $-\log_{10}(p)$ values from F-tests of scaffold-level means; bars exceeding the dashed $\alpha = 0.05$ threshold indicate statistically significant differences. (B) Accuracy comparison based on Welch's t-statistics from independent-samples t-tests of scaffold-level means; significant comparisons are highlighted in red.

pipeline demonstrated here executes a single, fixed-parameter G-code path rather than exposing tunable, per-segment process control.

Table 7. Itemized build cost of the retrofitted platform compared with the commercial BioBot list price

Item	Cost (USD)
Component	
IRB 120T arm & IRC5 Compact controller	$16,000
Pneumatic system (solenoid, air tank, compressor)	$330
Solenoid control circuit (diode, MOSFET, wiring)	$15
Print bed (aluminum extrusion, glass, brackets)	$18
Extruder tooling (bracket, syringe holder)	$56.50
Electronics (Raspberry Pi, Arduino)	$197.50
Total, retrofitted platform	$16,617
Commercial BioAssemblyBot 400 (list price)	$160,000

Note: OctoPrint, CuraSlicer, and Python are free or open-source, and RAPID is included with the ABB IRC5 controller; none adds cost.

It is also worth noting that the BioBot's HMI, while capable, is not always straightforward for a user to reconfigure with custom toolpath geometries or process-parameter schedules—a rigidity the retrofitted platform's open, code-level access to every process parameter is specifically positioned to address. The retrofitted platform's total build cost was $16,617 (Table 7), an 89.6% reduction relative to the BioBot's $160,000 list price—a savings of $143,383 in capital cost. That cost gap should be read alongside the feature gap just described: the BioBot's price also buys a validated HMI, vendor support, and, depending on configuration, integrated peripherals such as a monitoring camera or a UV-crosslinking module that the present retrofit does not yet include.

The retrofitted platform's open, TCP/IP-based command architecture makes adding comparable open-source hardware—an alternate extruder, an in-line monitoring camera, an additional UV-crosslinking stage—a natural, low-cost extension rather than a redesign, but that integration work has not yet been done and is not claimed here. Framed this way, the intent of this comparison is not to declare the retrofitted platform an outright replacement for a mature commercial system on the strength of a single, bi-layer acellular validation study. Given how limited the present dataset is, the finding that a $16,617 retrofit of a general-purpose industrial arm matches or exceeds the $160,000 BioBot on repeatability and pore-scale accuracy is itself the notable result, and one that should be credited substantially to the ABB IRB 120T's native positioning accuracy as a high-precision industrial manipulator rather than to any advantage in process sophistication over the commercial system. The retrofitted platform is best positioned, on this evidence, as a fundamental, accessible starting point for robot-assisted bioprinting—one that trades the BioBot's polish, support, and packaged feature set for full user-level control over process parameters and open hardware integration—rather than as a finished, feature-complete competitor.

4. Discussion

The gap motivating this work was the absence of a system combining industrial-robot-grade repeatability, a real-time and open-source G-code-to-RAPID pipeline compatible with the existing FDM slicer ecosystem, and a statistically rigorous comparison against a commercial robotic bioprinting benchmark. The results in **Section 3** close that gap directly: the retrofitted ABB IRB 120T platform reproduced print dimensions with significantly lower macro-scale (overall-dimension) variance than the commercial BioBot, and a numerically lower, though not always statistically significant, pore-scale variance at the scaffold level (Figure 14), showed no statistically significant difference from the BioBot in overall-dimension or pore-width accuracy, and exceeded its pore-length accuracy in the pooled analysis—all at an 89.6% lower capital cost. Taken together, these results support the central claim of this work: retrofitting an existing, unmodified industrial robot is a technically viable and substantially lower-cost alternative to purpose-built or fully custom robotic bioprinting hardware.

4.1. Under-extrusion as a material and process-parameter dependent variable

Every measured feature on both platforms was undersized relative to its STL target (Figure 9), and the ANOVA (Figure 11) attributes none of this systematic offset essentially to the robot's motion control: neither the print-run blocking factor nor the deposition-direction factor was significant, meaning dimensions did not drift from print to print and were not biased by which axis the robot moved along. The analysis implicates process chemistry and pressure: A_4C_4 was extruded from the retrofitted platform at 17 psi (117.2 kPa; nominal: 14 psi [96.53 kPa]) and from the BioBot at 15 psi (103.42 kPa), in both cases without ionic or photo-induced crosslinking. An uncrosslinked, shear-thinning hydrogel extruded above its nominal pressure will overflow at the nozzle and continue to spread laterally under its own weight after deposition, narrowing pore openings and contracting outer boundaries—exactly the uniform, direction-independent undersizing observed here. Framed this way, the dimensional-accuracy limitation identified in this study is a bioink/process-parameter characterization problem—matching pressure, feedrate, and crosslinking timing to the specific bioink batch and nozzle geometry—rather than evidence against the retrofit's kinematic fidelity. This distinction demonstrates that the proposed low-cost robotic retrofit satisfies the first essential requirement for robotic bioprinting: positional accuracy and repeatability comparable to the commercial benchmark evaluated here. Having established the mechanical and motion-control performance of the platform, subsequent improvements in dimensional fidelity can be addressed through bioink formulation and process-parameter optimization rather than additional hardware development.

It should be noted that robot positional accuracy is inferred here indirectly, from the dimensional repeatability of printed hydrogel scaffolds, rather than measured directly with independent metrology (e.g., a laser tracker or ballbar study of the end-effector path itself). The present results therefore demonstrate that the retrofitted platform can fabricate scaffolds with repeatability comparable to or better than the commercial benchmark; they should not be read as an independently validated measurement of the ABB IRB 120T's absolute positional accuracy under this control pipeline, which we identify as a distinct and valuable direction for future work.

The direction × dimension-class interaction (F = 9.38, p = 0.004) is consistent with this process-chemistry explanation: because the scaffold's X-direction (length) strands are deposited first and remain uncrosslinked and unconstrained while the Y-direction (width) strands are subsequently deposited on top of them, the first-laid strands have more time to relax and spread before any subsequent mechanical constraint is added. The practical implication is that in-line crosslinking—physical (co-extruded $CaCl_2$ through the printhead's existing Y-connector) or photo-based (the printhead's existing UV light-emitting diode [LED] ring)—should be the first process modification tested in follow-on work, ahead of any further hardware change, since the printhead already integrates both crosslinking pathways and neither was engaged in the present acellular validation prints.

Several mechanistic explanations discussed above and in Section 3, including viscoelastic die-swell, corner-transition velocity blending, motor-torque variation, and shear-rate effects, are proposed as plausible interpretations of the observed dimensional patterns. These mechanisms were not directly measured or independently validated in the present study. Pressure, crosslinking state, commanded-versus-executed trajectory, and bioink rheology were not experimentally varied in this study to isolate each one's individual contribution. Confirming these mechanisms would require, for example, logging commanded-versus-executed toolpaths, rheological characterization of the specific bioink batch, and a factorial design varying pressure and crosslinking independently; we identify this as a specific direction for future work rather than a conclusion drawn from the present dataset.

4.2. Repeatability and pore-scale accuracy advantages over the commercial benchmark

The retrofitted platform's lower dimensional variance

in the pooled, pore-level analysis across all four feature groupings (Figure 13)—a 60% lower mean SD and a 66% lower maximum range than the BioBot—is consistent with the sub-millimeter repeatability specification typical of ABB's IRB-class industrial arms. It also indicates that the G-code-to-RAPID translation pipeline preserves that native repeatability rather than degrading it; as detailed below, the corresponding scaffold-level (unit-appropriate) comparison found this advantage statistically significant only for the macro-scale overall-dimension grouping. The pore-length accuracy advantage (77.4% vs. 65.7% of target; pooled, pore-level one-sample comparison, $p < 0.001$; scaffold-level Welch's $t = 4.20$, $p = 0.041$, not significant after Holm–Bonferroni correction for multiple comparisons; Table 6) is more surprising given that both platforms were subject to the same over-extrusion/no-crosslinking process condition, and may reflect differences in nozzle geometry, printhead standoff distance, or toolpath dwell behavior at the small radius of the pore corners between the two systems; a direct nozzle- and toolpath-matched comparison would be needed to isolate the cause and is noted as a direction for future work. The Y-direction pore-width comparison, by contrast, showed no significant difference between platforms ($p = 0.210$), reinforcing that the retrofitted platform's advantage is concentrated in the direction-dependent (X/length) pore features rather than uniform across all fine-feature measurements.

As shown by the scaffold-level reanalysis (Section 3.4, Table 4), the retrofitted platform exhibited numerically lower pore-scale variability, although this difference did not reach statistical significance when the analysis was restricted to independent scaffolds ($n = 5$ retrofit; $n = 3$ BioBot). At the scaffold level, a statistically significant repeatability advantage was observed only for the macro-scale overall dimensions. Both pooled and scaffold-level analyses are therefore reported to provide a comprehensive assessment of repeatability across measurement and scaffold levels.

4.3. The handshake latency behind the print-speed deficit

The retrofitted platform's roughly 21% longer print time and correspondingly lower hourly throughput (Section 3.5) are primarily attributable to the two-stage, block-and-wait software handshake in the G-code-to-RAPID pipeline (Section 2.3). Under this protocol, OctoPrint's sending thread is held at every command boundary until the robot controller confirms an EXECUTED signal, adding overhead at each toolpath transition that a continuously streamed, native RAPID path avoids. This tradeoff was an intentional design choice for this proof-of-concept system, prioritizing execution correctness and command order over speed validation. Additionally, a portion of this temporal discrepancy and observed variance stems from the system timer starting immediately upon RAPID program initiation, capturing the latency window prior to triggering print execution via the OctoPrint interface; although minimized during testing, this setup delay naturally inflates overall recorded durations. Looking ahead, replacing the block-and-wait handshake with a continuous, velocity-synchronized streaming protocol is a primary objective for future iterations—both to close the throughput gap with commercial printers and to eliminate stationary shear exposure for sensitive cell-laden bio-inks at nozzle transitions.

The communication architecture implemented in the present study performs on-the-fly, per-line G-code-to-RAPID translation and execution through the RobotSync pipeline. For the validation experiments, the data-logging framework recorded aggregate print duration using the OctoPrint and RAPID clocks; per-command handshake latency, command rate, and timing jitter at the individual G-code level were not recorded. To enable more detailed characterization of communication performance, future validation will incorporate direct logging of per-command latency, command rate, and timing jitter within the RobotSync pipeline. In this study, the term *real-time* therefore refers specifically to on-the-fly translation and execution of individual G-code commands, distinguishing the implemented approach from both offline path pre-computation and continuous, velocity-synchronized trajectory streaming.

4.4. Toward cell-laden and non-planar bioprinting

This work deliberately scoped its validation to acellular, planar-toolpath printing to isolate and rigorously test the G-code-to-RAPID translation pipeline and the resulting platform's dimensional performance before introducing the additional variability of living cells or non-planar geometry. With that kinematic and translational validation complete, three directions follow naturally. First, process-parameter characterization—operating at the nominal 14 psi (96.53 kPa) extrusion pressure and engaging the printhead's existing ionic and photo-crosslinking hardware[22]—should be revisited as the direct remedy for the systematic undersizing identified in Section 4.1, ahead of any further hardware modification. Second, replacing the block-and-wait handshake with a continuous, speed-synchronized streaming protocol (Section 4.3) would close the throughput gap with commercial systems and reduce dwell-related over-extrusion at path transitions, a prerequisite for reliable cell-laden printing. Third, the six-axis capability of the IRB 120T—used here only for planar, Cartesian-equivalent motion to isolate

the translation pipeline from confounding kinematic variables—is available for future non-planar and in situ toolpaths; combining this retrofit strategy with vision-based toolpath correction, as recently demonstrated for robotic bioprinting by Shojaei Barjuei *et al.*,[19] or with the flexible, endoscope-compatible *in situ* delivery strategies demonstrated by Thai *et al.*,[11] represents a natural extension once cell-laden process parameters are established. Each of these is a scoped, testable extension of the present platform rather than a new hardware program, a core advantage of a retrofitted system. Rather than repeat capital investments, subsequent capability gains are primarily software- and process-parameter-driven.

The contribution of this platform extends beyond demonstrating complex, non-planar geometries that cannot be fabricated using conventional Cartesian printers. Accordingly, the present work focuses on three primary contributions: (i) an open-source, real-time G-code-to-RAPID translation pipeline compatible with the conventional FDM slicer/G-code ecosystem; (ii) a statistically grounded dimensional benchmark against a commercial robotic bioprinter; and (iii) a validated six-axis mechanical and software framework—including tool-coordinate definition, workobject configuration, and RAPID motion routines—that can be extended to non-planar fabrication. Recent work by Shojaei Barjuei *et al.*[14] demonstrated the potential of six-axis robotic printing to reduce surface roughness by more than half for curved geometries using dynamic tool-orientation tracking compared with three-axis printing. Building on the planar validation established here, future work will therefore extend the retrofitted platform to non-planar and curved-surface scaffolds and quantitatively evaluate tool-orientation tracking and surface fidelity.

4.5. Limitations

The present study has several limitations that should be considered when interpreting the findings. Validation used a single acellular, uncrosslinked bioink formulation and a planar lattice geometry; therefore, the performance of the system with cell-laden bioinks, alternative material formulations, and non-planar printing remains to be evaluated. In addition, the relatively small and unequal sample sizes between the retrofitted and BioBot platforms ($n = 5$ and $n = 3$ scaffolds, respectively) limited the statistical power of the scaffold-level comparisons, particularly for assessing pore-scale variability. Dimensional characterization was based on single-operator image analysis at a resolution approaching the lower limit of the measurement system, and future studies incorporating multiple operators and repeated image acquisition would provide more comprehensive measurement-system validation.

The software and documentation package includes the RAPID and Python source code for the translation pipeline, the associated open-source license, a pinned dependency list, the CuraSlicer profile used to generate the G-code, example toolpaths, and hardware and wiring documentation for the extrusion-control circuit described in Section 2.2. The package also includes the raw scaffold images, ImageJ measurements underlying Sections 3.1–3.4, and analysis scripts used for the reported statistical analyses. Pipeline documentation describes the handling of unsupported G-code commands, coordinate and feedrate state tracking between commands, and the G0-to-MoveJ mapping described in Section 2.4. In the current implementation, interruption of a print initiates the error-handling routine, which homes the robot and terminates communication; however, the routine does not explicitly reset the doFan extrusion-control output. Explicit shutdown of this output following an interrupted print is therefore identified as a safety-related improvement for future implementation.

5. Conclusion

This work retrofitted a low-cost, previously non-bioprinting six-axis industrial robot (ABB IRB 120T/IRC5 Compact) into an open-source extrusion bioprinter by integrating an existing low-cost printhead, building a custom work cell and solenoid extrusion-control circuit, and developing a real-time OctoPrint plugin and RAPID program that translate standard slicer-generated G-code into robot motion over a two-stage TCP/IP handshake. Validation against a commercial robotic bioprinter (BioAssemblyBot 400) across five statistical tests—descriptive statistics, Gage R&R, one-sample *t*-tests, ANOVA, and cross-platform *F*-tests/independent-samples *t*-tests—showed that the retrofitted platform achieved significantly lower macro-scale dimensional (overall-dimension) variance than the commercial system, and a numerically lower but not always statistically significant pore-scale variance at the small per-platform sample sizes tested (mean CVs 2.25% vs. 5.07%), showed no statistically significant difference from the BioBot in overall-dimension or pore-width accuracy, and exceeded its pore-length accuracy in the pooled, pore-level analysis (77.4% vs. 65.7% of target, $p < 0.001$; the corresponding scaffold-level comparison gave Welch's $t = 4.20$, $p = 0.041$, which does not survive correction for multiple comparisons across the four feature groupings tested; see Section 3.4 and Table 4). This performance was achieved at a total build cost of $16,617, an 89.6% reduction relative to the BioBot's $160,000 list price. The ANOVA (Section 3.3) attributed essentially none of the systematic dimensional undersizing observed on both platforms

to the robot's motion control (print-run and directional effects were not significant); consistent with this, extrusion pressure and the absence of crosslinking are identified as the most likely process-parameter explanations (Section 4.1), rather than the robot's motion control, identifying bioink process-parameter characterization as the next step toward dimensionally accurate, cell-laden printing on this platform. Together, these results demonstrate that retrofitting existing industrial robots is a viable, substantially lower-cost pathway to multi-axis robotic bioprinting, and they provide a validated software and hardware foundation for future non-planar, *in situ*, and cell-laden extensions of the platform.

Acknowledgments

The authors acknowledge the College of Engineering Technology, Rochester Institute of Technology, for providing laboratory space and access to the ABB IRB 120T robotic arm and IRC5 controller used in this study.

Funding

The authors received no financial support for the research, authorship, and/or publication of this article.

Conflict of interest

The authors declare they have no competing interests.

Author contributions

Conceptualization: Ahasan Habib
Data curation: Kenneth Houston, Perrin Woods, Ahasan Habib
Investigation: Kenneth Houston, Perrin Woods
Methodology: Kenneth Houston, Perrin Woods, Ahasan Habib
Project administration: Ahasan Habib
Software: Kenneth Houston, Perrin Woods
Supervision: Ahasan Habib
Validation: Kenneth Houston, Perrin Woods, Ahasan Habib
Writing – original draft: Ahasan Habib, Kenneth Houston
Writing – review & editing: Ahasan Habib, Kenneth Houston, Perrin Woods

Ethics approval and consent to participate

Not applicable. This study did not involve human participants, animal subjects, or primary cell lines from human patients; all validation prints used an acellular hydrogel bioink.

Consent for publication

Not applicable.

Availability of data

The per-scaffold, per-feature dimensional measurements for both platforms and the strand-width correction measurements analyzed in this study, together with the RobotSync OctoPrint plugin, fake-firmware emulator, and RAPID modules described in Section 2.3, will be available from the corresponding author upon reasonable request.

AI tools statement

None.

References

1. Mandrycky C, Wang Z, Kim K, Kim DH. 3D bioprinting for engineering complex tissues. *Biotechnol Adv*. 2016;34(4):422-434.

   doi: 10.1016/j.biotechadv.2015.12.011

2. Naghieh S, Chen X. Printability—a key issue in extrusion-based bioprinting. *J Pharm Anal*. 2021;11(5):564-579.

   doi: 10.1016/j.jpha.2021.02.001

3. Amorim PA, d'Ávila MA, Anand R, Moldenaers P, Van Puyvelde P, Bloemen V. Insights on shear rheology of inks for extrusion-based 3D bioprinting. *Bioprinting*. 2021;22:e00129.

   doi: 10.1016/j.bprint.2021.e00129

4. Rohauer R, Schimmelpfennig K, Mei V, Woods P, Lewis CL, Habib MA. Characterization and prediction of properties of polymeric materials for extrusion-based bioprinting process. In: *Proceedings of ASME 2025 20th International Manufacturing Science and Engineering Conference (MSEC2025)*. Vol 1. New York, NY: American Society of Mechanical Engineers; 2025.

   doi: 10.1115/MSEC2025-155176

5. Strauß S, Schroth B, Hubbuch J. Evaluation of the reproducibility and robustness of extrusion-based bioprinting processes applying a flow sensor. *Front Bioeng Biotechnol*. 2022;10:831350.

   doi: 10.3389/fbioe.2022.831350

6. Kirchmajer DM, Gorkin R 3rd. An overview of the suitability of hydrogel-forming polymers for extrusion-based 3D-printing. *J Mater Chem B*. 2015;3(20):4105-4117.

   doi: 10.1039/C5TB00393H

7. Boularaoui S, Al Hussein G, Khan KA, Christoforou N, Stefanini C. An overview of extrusion-based bioprinting with a focus on induced shear stress and its effect on cell viability. *Bioprinting*. 2020;20:e00093.

   doi: 10.1016/j.bprint.2020.e00093

8. Kačarević ŽP, Rider PM, Alkildani S, *et al*. An introduction to 3D bioprinting: possibilities, challenges and future aspects. *Materials (Basel)*. 2018;11(11):2199.

doi: 10.3390/ma11112199

9. Kahl M, Gertig M, Hoyer P, Friedrich O, Gilbert DF. Ultra-low-cost 3D bioprinting: modification and application of an off-the-shelf desktop 3D-printer for biofabrication. *Front Bioeng Biotechnol*. 2019;7:184.

   doi: 10.3389/fbioe.2019.00184

10. Tong A, Pham QL, Abatemarco P, *et al*. Review of low-cost 3D bioprinters: state of the market and observed future trends. *SLAS Technol*. 2021;26(4):333-366.

    doi: 10.1177/24726303211020297

11. Thai MT, Phan PT, Tran HA, *et al*. Advanced soft robotic system for in situ 3D bioprinting and endoscopic surgery. *Adv Sci (Weinh)*. 2023;10(12):2205656.

    doi: 10.1002/advs.202205656

12. Urhal P, Weightman A, Diver C, Bartolo P. Robot assisted additive manufacturing: a review. *Robot Comput Integr Manuf*. 2019;59:335-345.

    doi: 10.1016/j.rcim.2019.05.005

13. Vasques CMA, Figueiredo FAV. The 3D-printed low-cost delta robot Oscar: technology overview and benchmarking. *Eng Proc*. 2021;11(1):43.

    doi: 10.3390/ASEC2021-11173

14. Shojaei Barjuei E, Shin J, Kim K, Lee J. High-precision multi-axis robotic printing: optimized workflow for complex tissue creation. *Bioengineering (Basel)*. 2025;12(9):949.

    doi: 10.3390/bioengineering12090949

15. Yang S, Kim H, Rezayof O, *et al*. Development and quantitative evaluation of a novel autonomous in situ bioprinting surgical robotic framework for treatment of volumetric muscle loss injuries. *IEEE Trans Autom Sci Eng*. 2025;22:2565-2576.

    doi: 10.1109/TASE.2024.3382200

16. Albrecht FB, Schmidt FF, Schmidt C, Börret R, Kluger PJ. Robot-based 6D bioprinting for soft tissue biomedical applications. *Eng Life Sci*. 2024;24(7):e2300226.

    doi: 10.1002/elsc.202300226

17. Fortunato GM, Batoni E, Pasqua I, Nicoletta M, Vozzi G, De Maria C. Automatic photo-cross-linking system for robotic-based in situ bioprinting. *ACS Biomater Sci Eng*. 2023;9(12):6926-6934.

    doi: 10.1021/acsbiomaterials.3c00898

18. Fortunato GM, Sigismondi S, Nicoletta M, *et al*. Analysis of the robotic-based in situ bioprinting workflow for the regeneration of damaged tissues through a case study. *Bioengineering (Basel)*. 2023;10(5):560.

    doi: 10.3390/bioengineering10050560

19. Shojaei Barjuei E, Shin J, Kim K, Lee J. Precision improvement of robotic bioprinting via vision-based tool path compensation. *Sci Rep*. 2024;14(1):17764.

    doi: 10.1038/s41598-024-68597-z

20. Ribeiro FM, Pires JN, Azar AS. Implementation of a robot control architecture for additive manufacturing applications. *Ind Robot*. 2019;46(1):73-82.

    doi: 10.1108/IR-11-2018-0226

21. ABB. *Application Manual: 3D Printing*. Document ID 3HAC073941-001. Zurich, Switzerland: ABB; 2024. Accessed November 13, 2026. https://library.abb.com/d/3HAC073941-001

22. Nilsson D. G-code to RAPID translator for RobotStudio. 2016.

23. Pan J, Fu Z, Xiong J, Lei X, Zhang K, Chen X. RobMach: G-code-based off-line programming for robotic machining trajectory generation. *Int J Adv Manuf Technol*. 2022;118(7):2497-2511.

    doi: 10.1007/s00170-021-08082-3

24. Woods P, Smith C, Clark S, Habib A. Integrating pneumatic and thermal control in 3D bioprinting for improved bio-ink handling. *Designs*. 2024;8(4):83.

    doi: 10.3390/designs8040083

25. Woods P, Houston K, Sakib N, Lewis CL, Habib A. From gantry systems to robotic arms: a versatile hybrid 3D bioprinting nozzle with real-time UV curing. In: *Proceedings of ASME 2025 20th International Manufacturing Science and Engineering Conference (MSEC2025)*. Vol 1. New York, NY: American Society of Mechanical Engineers; 2025.

    doi: 10.1115/MSEC2025-155441

26. UltiMaker. *Cura Software*. Version 5.5.0. Geldermalsen, Netherlands: UltiMaker. Accessed November 13, 2026. https://ultimaker.com/software/ultimaker-cura/

27. Khoda B, Habib MA. 3D bioprinting with cellulose-derived bio-ink and precursors. In: Klemmt C, Beaucage G, eds. *Biodegradable 3D-Printing*. Singapore: Springer; 2026:71-98.

    doi: 10.1007/978-981-95-4025-9_5

28. Habib A, Sathish V, Mallik S, Khoda B. 3D printability of alginate-carboxymethyl cellulose hydrogel. *Materials (Basel)*. 2018;11(3):454.

    doi: 10.3390/ma11030454